NUMERICAL INVESTIGATION OF VORTEX FORMATION AT SINGLE AND MULTIPLE SYMMETRIC HORIZONTAL INTAKES

A THESIS SUBMITTED TO
THE GRADUATE SCHOOL OF NATURAL AND APPLIED SCIENCES
OF
MIDDLE EAST TECHNICAL UNIVERSITY

BY

UMUT AYKAN

IN PARTIAL FULFILLMENT OF THE REQUIREMENTS
FOR
THE DEGREE OF MASTER OF SCIENCE
IN
CIVIL ENGINEERING

APRIL 2024

Approval of the thesis:

NUMERICAL INVESTIGATION OF VORTEX FORMATION AT SINGLE AND MULTIPLE SYMMETRIC HORIZONTAL INTAKES

submitted by **UMUT AYKAN** in partial fulfillment of the requirements for the degree of **Master of Science in Civil Engineering Department, Middle East Technical University** by,

Prof. Dr. Naci Emre Altun
Dean, **Graduate School of Natural and Applied Sciences** _____

Prof. Dr. Erdem Canbay
Head of the Department, **Civil Engineering** _____

Prof. Dr. Mete Köken
Supervisor, **Civil Engineering, METU** _____

Examining Committee Members:

Assoc. Prof. Dr. Ali Ercan
Civil Engineering, METU _____

Prof. Dr. Mete Köken
Civil Engineering, METU _____

Assoc. Prof. Dr. Elif Oğuz
Civil Engineering, METU _____

Assist. Prof. Dr. Cüneyt Baykal
Civil Engineering, METU _____

Assist. Prof. Dr. Önder Koçyiğit
Civil Engineering, Gazi University _____

Date: 26.04.2024

I hereby declare that all information in this document has been obtained and presented in accordance with academic rules and ethical conduct. I also declare that, as required by these rules and conduct, I have fully cited and referenced all material and results that are not original to this work.

Name, Last name: Umut Aykan

Signature:

ABSTRACT

NUMERICAL INVESTIGATION OF VORTEX FORMATION AT SINGLE AND MULTIPLE SYMMETRIC HORIZONTAL INTAKES

Aykan, Umut

M.S., Department of Civil Engineering

Supervisor: Prof. Dr. Mete Köken

April 2024, 80 pages

There is not a generalized equation in literature to identify critical submergence depth at single and multiple symmetric horizontal intakes. Existing equations often rely on some special cases and assumptions. Development of computational power in recent years allows simulation of these complex flows. In this study, vortex formation in symmetrical horizontal water intake structures composed of single and multiple intakes are investigated with a software using 3D numerical modelling named Flow-3D. Single, double, and triple intakes at different discharges are simulated and the depth of critical submergence which the air core vortex formation is observed for each case is specified and compared with the physical experimental results. Numerical simulations are consistently under estimating the critical submergence depth compared to the experimental results. It was observed that as the discharge increases critical submergence depth increases for single, double and triple intakes. It was also observed that for the similar intake discharges triple intakes have larger critical submergence depth than the double intakes.

Keywords: Single and multiple symmetric horizontal intakes, Air-entraining vortices, Vortex formation, Critical submergence, Flow-3D

ÖZ

TEKLİ VE ÇOKLU SİMETRİK YATAY SU ALMA YAPILARINDA VORTEKS OLUŞUMUNUN SAYISAL OLARAK İNCELENMESİ

Aykan, Umut
Yüksek Lisans, İnşaat Mühendisliği Bölümü
Tez Yöneticisi: Prof. Dr. Mete Köken
Nisan 2024, 80 sayfa

Tekli ve çoklu simetrik yatay su alma yapılarında kritik batıklığı belirlemek için literatürde geçerli bir denklem yoktur. Mevcut denklemler bazı özel durumlara ve varsayımlara dayanarak kullanılabilmektedir. Son yıllarda bilgisayar hesaplama gücünün gelişmesi, bu karmaşık akışların simülasyonuna olanak sağlamaktadır. Bu çalışmada, tek ve çoklu alımlardan oluşan simetrik yatay su alma yapılarında vorteks oluşumu, Flow-3D adlı 3D sayısal modelleme programı kullanılarak gözlemlenmiştir. Farklı debilerdeki tek, çift ve üçlü su alma ağızları modellenip her bir durum için vorteks oluşumunun gözlemlendiği kritik batıklık belirlenmiş ve fiziksel deney sonuçlarıyla kıyaslanmıştır. Sayısal simülasyonlar fiziksel deney sonuçlarına göre kritik batıklığı sürekli olarak daha düşük bulmaktadır. Debinin artmasıyla tekli, ikili ve üçlü su alma yapılarında kritik batıklığın da arttığı gözlemlenmiştir. Ayrıca benzer debilerde üçlü su alma yapılarının ikili su alma yapılarına göre daha büyük kritik batıklık derinliğine sahip olduğu gözlemlenmiştir.

Anahtar Kelimeler: Tekli ve çoklu simetrik yatay su alma yapıları, Hava girişli girdaplar, Vorteks oluşumu, Kritik batıklık derinliği, Flow-3D

To my family

ACKNOWLEDGEMENTS

I would like to give my special thanks to my supervisor Prof. Dr. Mete KÖKEN for his assistance, support, and patience during my study.

I would like to express my appreciation to Alper SUNGUR for his advice, helpfulness, and friendship during my study period.

The experimental results were taken from the study of Serkan Gökmener which was supported by TUBITAK under Project No: 113M326.

TABLE OF CONTENTS

ABSTRACT v

ÖZ vi

ACKNOWLEDGEMENTS viii

TABLE OF CONTENTS ix

LIST OF TABLES xi

LIST OF FIGURES xii

LIST OF SYMBOLS xvii

CHAPTERS

1. INTRODUCTION 1

    1.1 Intakes 1

    1.2 Definition of Vortex 2

    1.3 Vortex-Related Issues 3

    1.4 Critical Submergence Depth 3

    1.5 Guidelines to Prevent Vortex Formation 4

    1.6 Scope of The Study 5

2. LITERATURE REVIEW 9

3. NUMERICAL MODELLING 17

    3.1 Introduction 17

    3.2 Model Configuration 17

    3.3 Simulation Procedure 24

    3.4 Viscous Solver 26

    3.5 Grid Size Dependency 27

4. RESULTS OF ANALYSES 29

4.1 Introduction....29
4.2 Analysis....29
4.3 Comparison of Physical Experiments and Numerical Simulation Results 30
4.4 Comparison of Critical Submergence and Number of Intakes....33
4.5 Comparison of Critical Submergence and Discharge....33
4.6 Location of the Air Core Vortex....35
5. CONCLUSIONS....37
REFERENCES....39
APPENDICES....43
A. NUMERICAL SIMULATION RESULTS....43

LIST OF TABLES

TABLES

Table 3.1 PC specifications 26
Table 3.2 Simulations 26
Table 3.3 Grid size dependency comparison 28
Table 4.1 Experimental and numerical simulation results 31
Table 4.2 Numerical simulation discrepancy margins 32

LIST OF FIGURES

FIGURES

Figure 1.1 Types of vortices (Knauss, 1987) 2
Figure 1.2 Vortex sources (Durgin & Hecker, 1978) 3
Figure 1.3 Critical Submergence Depth 4
Figure 1.4 View of Gökmener's (2016) model from dowstream (taken from Gökmener (2016)) 6
Figure 1.5 Close view of Gökmener's (2016) triple water intake structure model from dowstream (taken from Gökmener (2016)) 7
Figure 2.1 Recommended depth of submergence (Knauss, 1987) 11
Figure 3.1 Model members 19
Figure 3.2 Single intake structure with dimensioning 20
Figure 3.3 Double intake structure with dimensioning 20
Figure 3.4 Triple intake structure with dimensioning 21
Figure 3.5 Coarse and fine mesh blocks 22
Figure 3.6 Boundary conditions 23
Figure 3.7 Simulation flowchart 25
Figure 4.1 Depth of critical submergence and discharge values for all setups with available results of both numerical and physical experiments 32
Figure 4.2 Depth of critical submergence and number of intake values of physical experiment and numerical simulation results for given discharge values 33
Figure 4.3 Depth of critical submergence and discharge values of physical experiment and numerical simulation results 34
Figure A.1 Case-01 z-axis vorticity (ωz, 1/sec) at the free water surface 43
Figure A.2 Case-01 z-axis vorticity (ωz, 1/sec) slightly beneath the observable vortex core 43
Figure A.3 Case-01 z-axis vorticity (ωz, 1/sec) at mid-S_c level (59.50 cm) 44
Figure A.4 Case-01 3D streamlines and isosurfaces of the air-water interface cross-section (longitudinal (y) direction) 44
Figure A.5 Case-01 3D streamlines and isosurfaces of the air-water interface cross-section (transverse (x) direction) 45
Figure A.6 Case-02 z-axis vorticity (ωz, 1/sec) at the free water surface 45

Figure A.7 Case-02 z-axis vorticity (ωz, 1/sec) slightly beneath the observable vortex core 46
Figure A.8 Case-02 z-axis vorticity (ωz, 1/sec) at mid-S_c level (57.00 cm)..... 46
Figure A.9 Case-02 3D streamlines and isosurfaces of the air-water interface cross-section (longitudinal (y) direction) 47
Figure A.10 Case-02 3D streamlines and isosurfaces of the air-water interface cross-section (transverse (x) direction) 47
Figure A.11 Case-03 z-axis vorticity (ωz, 1/sec) at the free water surface 48
Figure A.12 Case-03 z-axis vorticity (ωz, 1/sec) slightly beneath the observable vortex core 48
Figure A.13 Case-03 z-axis vorticity (ωz, 1/sec) at mid-S_c level (55.75 cm)..... 49
Figure A.14 Case-03 3D streamlines and isosurfaces of the air-water interface cross-section (longitudinal (y) direction) 49
Figure A.15 Case-03 3D streamlines and isosurfaces of the air-water interface cross-section (transverse (x) direction) 50
Figure A.16 Case-4 z-axis vorticity (ωz, 1/sec) at the free water surface 50
Figure A.17 Case-04 z-axis vorticity (ωz, 1/sec) slightly beneath the observable vortex core 51
Figure A.18 Case-04 z-axis vorticity (ωz, 1/sec) at mid-S_c level (47.00 cm)..... 51
Figure A.19 Case-04 3D streamlines and isosurfaces of the air-water interface cross-section (longitudinal (y) direction) 52
Figure A.20 Case-004 3D streamlines and isosurfaces of the air-water interface cross-section (transverse (x) direction) 52
Figure A.21 Case-05 z-axis vorticity (ωz, 1/sec) at the free water surface 53
Figure A.22 Case-05 z-axis vorticity (ωz, 1/sec) slightly beneath the observable vortex core 53
Figure A.23 Case-05 z-axis vorticity (ωz, 1/sec) at mid-S_c level (47.00 cm)..... 54
Figure A.24 Case-05 3D streamlines and isosurfaces of the air-water interface cross-section (longitudinal (y) direction) 54
Figure A.25 Case-05 3D streamlines and isosurfaces of the air-water interface cross-section (transverse (x) direction) 55
Figure A.26 Case-06 z-axis vorticity (ωz, 1/sec) at the free water surface 55
Figure A.27 Case-06 z-axis vorticity (ωz, 1/sec) slightly beneath the observable vortex core 56

Figure A.28 Case-06 z-axis vorticity (ωz, 1/sec) at mid-S_c level (43.25 cm) 56
Figure A.29 Case-06 3D streamlines and isosurfaces of the air-water interface cross-section (longitudinal (y) direction) 57
Figure A.30 Case-06 3D streamlines and isosurfaces of the air-water interface cross-section (transverse (x) direction) 57
Figure A.31 Case-07 z-axis vorticity (ωz, 1/sec) at the free water surface 58
Figure A.32 Case-07 z-axis vorticity (ωz, 1/sec) slightly beneath the observable vortex core 58
Figure A.33 Case-07 z-axis vorticity (ωz, 1/sec) at mid-S_c level (40.75 cm) 59
Figure A.34 Case-07 3D streamlines and isosurfaces of the air-water interface cross-section (longitudinal (y) direction) 59
Figure A.35 Case-07 3D streamlines and isosurfaces of the air-water interface cross-section (transverse (x) direction) 60
Figure A.36 Case-08 z-axis vorticity (ωz, 1/sec) at the free water surface 60
Figure A.37 Case-08 z-axis vorticity (ωz, 1/sec) slightly beneath the observable vortex core 61
Figure A.38 Case-08 z-axis vorticity (ωz, 1/sec) at mid-S_c level (38.25 cm) 61
Figure A.39 Case-08 3D streamlines and isosurfaces of the air-water interface cross-section (longitudinal (y) direction) 62
Figure A.40 Case-08 3D streamlines and isosurfaces of the air-water interface cross-section (transverse (x) direction) 62
Figure A.41 Case-09 z-axis vorticity (ωz, 1/sec) at the free water surface 63
Figure A.42 Case-09 z-axis vorticity (ωz, 1/sec) slightly beneath the observable vortex core 63
Figure A.43 Case-09 z-axis vorticity (ωz, 1/sec) at mid-S_c level (37.00 cm) 64
Figure A.44 Case-09 3D streamlines and isosurfaces of the air-water interface cross-section (longitudinal (y) direction) 64
Figure A.45 Case-09 3D streamlines and isosurfaces of the air-water interface cross-section (transverse (x) direction) 65
Figure A.46 Case-10 z-axis vorticity (ωz, 1/sec) at the free water surface 65
Figure A.47 Case-10 z-axis vorticity (ωz, 1/sec) slightly beneath the observable vortex core 66
Figure A.48 Case-10 z-axis vorticity (ωz, 1/sec) at mid-S_c level (34.50 cm) 66

Figure A.49 Case-10 3D streamlines and isosurfaces of the air-water interface cross-section (longitudinal (y) direction) 67
Figure A.50 Case-10 3D streamlines and isosurfaces of the air-water interface cross-section (transverse (x) direction) 67
Figure A.51 Case-11 z-axis vorticity (ωz, 1/sec) at the free water surface 68
Figure A.52 Case-11 z-axis vorticity (ωz, 1/sec) slightly beneath the observable vortex core 68
Figure A.53 Case-11 z-axis vorticity (ωz, 1/sec) at mid-S_c level (45.75 cm)..... 69
Figure A.54 Case-11 3D streamlines and isosurfaces of the air-water interface cross-section (longitudinal (y) direction) 69
Figure A.55 Case-11 3D streamlines and isosurfaces of the air-water interface cross-section (transverse (x) direction) 70
Figure A.56 Case-12 z-axis vorticity (ωz, 1/sec) at the free water surface 70
Figure A.57 Case-12 z-axis vorticity (ωz, 1/sec) slightly beneath the observable vortex core 71
Figure A.58 Case-12 z-axis vorticity (ωz, 1/sec) at mid-S_c level (44.50 cm)..... 71
Figure A.59 Case-12 3D streamlines and isosurfaces of the air-water interface cross-section (longitudinal (y) direction) 72
Figure A.60 Case-12 3D streamlines and isosurfaces of the air-water interface cross-section (transverse (x) direction) 72
Figure A.61 Case-13 z-axis vorticity (ωz, 1/sec) at the free water surface 73
Figure A.62 Case-13 z-axis vorticity (ωz, 1/sec) slightly beneath the observable vortex core 73
Figure A.63 Case-13 z-axis vorticity (ωz, 1/sec) at mid-S_c level (42.00 cm)..... 74
Figure A.64 Case-13 3D streamlines and isosurfaces of the air-water interface cross-section (longitudinal (y) direction) 74
Figure A.65 Case-13 3D streamlines and isosurfaces of the air-water interface cross-section (transverse (x) direction) 75
Figure A.66 Case-14 z-axis vorticity (ωz, 1/sec) at the free water surface 75
Figure A.67 Case-14 z-axis vorticity (ωz, 1/sec) slightly beneath the observable vortex core 76
Figure A.68 Case-14 z-axis vorticity (ωz, 1/sec) at mid-S_c level (38.25 cm)..... 76
Figure A.69 Case-14 3D streamlines and isosurfaces of the air-water interface cross-section (longitudinal (y) direction) 77

Figure A.70 Case-14 3D streamlines and isosurfaces of the air-water interface cross-section (transverse (x) direction) 77
Figure A.71 Case-15 z-axis vorticity (ωz, 1/sec) at the free water surface 78
Figure A.72 Case-15 z-axis vorticity (ωz, 1/sec) slightly beneath the observable vortex core 78
Figure A.73 Case-15 z-axis vorticity (ωz, 1/sec) at mid-S_c level (38.25 cm) 79
Figure A.74 Case-15 3D streamlines and isosurfaces of the air-water interface cross-section (longitudinal (y) direction) 79
Figure A.75 Case-15 3D streamlines and isosurfaces of the air-water interface cross-section (transverse (x) direction) 80

LIST OF SYMBOLS

SYMBOLS

b	Distance between the center of the intakes and the side wall
D	Diameter of intake structure
Fr	Froude number of intake structure
h	Water depth at the reservoir of the intake
Δh_s	Water depth increment
Q	Inflow/Outflow discharge
S_c	Critical submergence depth measured from the summit point of intake pipe
S_c-exp	S_c measured in experimental study
t	Time
ω_z	Vorticity around z axis
z	Location of x-y plane on z axis
μ	Dynamic viscosity of the fluid
Γ	Circulation

CHAPTER 1

INTRODUCTION

1.1 Intakes

Inlet or intake structures serve the purpose of gathering high-quality water from various sources like rivers, lakes, or dam reservoirs. They are employed for purposes like:

- Drinking water
- Irrigation
- Power production
- Transportation
- Blocking debris
- Control gates
- Fish passages.

Intake structures do not adhere to standardized designs, as each design is distinct and can vary based on project-specific factors like hydraulic, geologic, topologic, and economic considerations. Nevertheless, some general design principles can be applied, including:

a) Designing the geometry of the intake structure in a way that minimizes hydraulic losses.
b) Ensuring that the elevation of the intake structure is positioned above the reservoir or lake's sedimentation level.
c) Setting the intake structure elevation by taking into account the critical submergence depth.

As a result, sedimentation and critical submergence depth emerge as crucial considerations in the design of intake structures.

1.2 Definition of Vortex

In situations of shallow submersion, vortices emerge at the intake structure's reservoir. The term "vortex" refers to the organized structure arising from circular streamlines and rotational flow.

Knauss (1987) visually categorizes vortices based on their strength intensity, as illustrated in Figure 1.1.

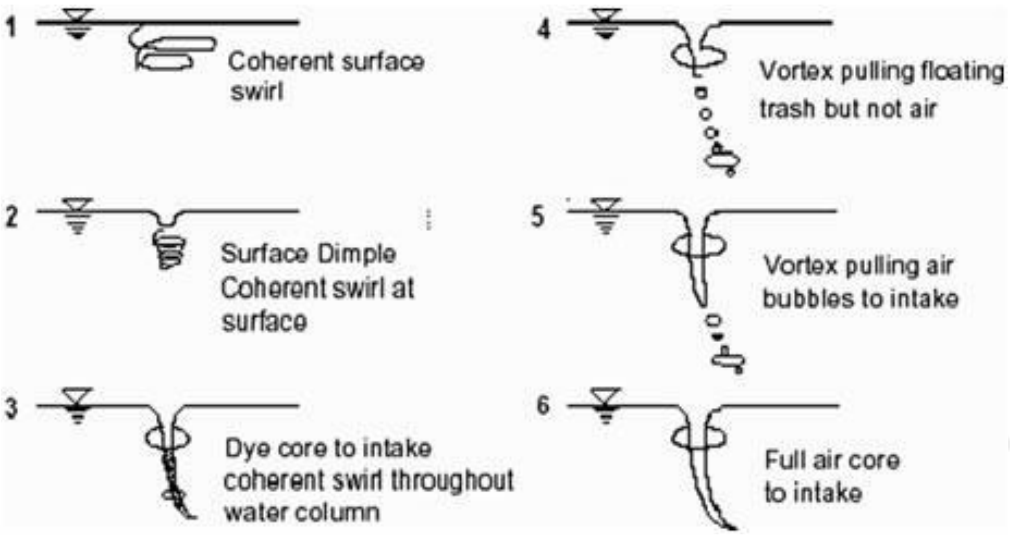

Figure 1.1 Types of vortices (Knauss, 1987)

Based on the research conducted by Durgin and Hecker in 1978, vortices are caused by three primary factors (Figure 1.2);

a) Asymmetry in the incoming flow pattern
b) Irregularities in the approach flow
c) Obstacles like piers or walls

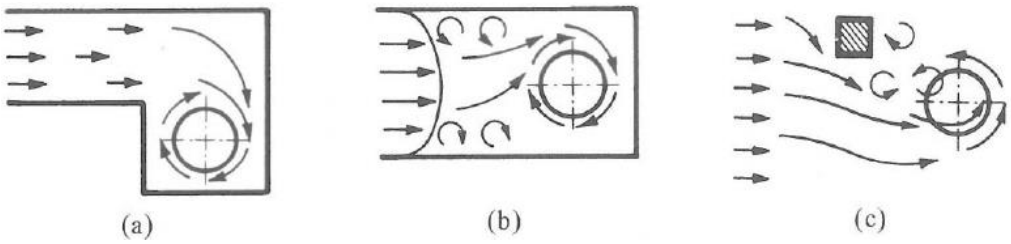

Figure 1.2 Vortex sources (Durgin & Hecker, 1978)

1.3 Vortex-Related Issues

Intakes are crafted by taking into account the calculated depth of critical submergence. If the depth of the intake falls below this critical value, various unfavorable scenarios may unfold, including:

- Air entrainment
- Cavitation
- Structural stresses
- Vibrations leading to decrease the lifetime of machinery components
- Decrease in discharge capacity
- Increase in head losses
- Entrainment of floating materials

1.4 Critical Submergence Depth

The depth of critical submergence is defined as the separation between the inlet structure and the top of water surface, observed right before the commencement of the vortices. Various researchers employ different reference points for the intake. The reference points commonly utilized in the literature are either the peak point of the intake structure's mouth or the mid-point of the intake structure.

Due to the unique characteristics of each intake design in practice, there is no precise mathematical expression in the current literature for calculating the critical submergence depth across various intake types. In this study critical submergence depth is taken as the maximum distance between the peak point of the intake structure's mouth and the top of water surface when an air-core vortex is present as illustrated in Figure 1.3.

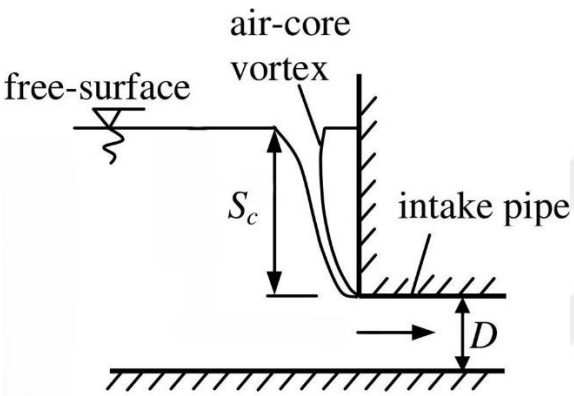

Figure 1.3 Critical Submergence Depth

1.5 Guidelines to Prevent Vortex Formation

There exists three ways to prevent vortex formation; adjusting the characteristics of approach flow, employing the anti-vortex devices, or improving the intake structure geometry.

These can be done by;

- Enhancing approach flow acceleration through geometry adjustments like increasing the approach channel width to decrease the approach velocity
- Implementing geometrical changes for uniformity
- Use of streamlines by piers or walls

- Utilizing gate control mechanisms
- Utilizing approach channels that guide the flow toward the intake
- Decreasing the elevation of intake to increase the depth of submergence
- Increasing the depth of tailwater submergence
- Implementing a structure which is laying horizontal above the intake
- Implementing floating rafts and flow straighteners.

1.6 Scope of The Study

The objective of this study is to assess the applicability of a software named Flow-3D in predicting the depth of critical submergence for symmetrical horizontal inlet structures. In order to accomplish this, results obtained from Flow-3D simulations is compared with the depths found in an experimental study conducted by Gökmener (2016). The study involved examining intakes to find out the depth of critical submergence for numerous horizontal intake settlements by adjusting the side walls of the setup. Views of Gökmener's (2016) model are given in Figure 1.4 and 1.5.

There is not any numerical study in the literature for multiple intakes. This study will be the first one for multiple intakes. In the current research, a numerical model replicating Gökmener's (2016) experimental setup was developed. 3D numerical simulations were performed using Flow-3D computational fluid dynamics software.

Figure 1.4 View of Gökmener's (2016) model from dowstream (taken from Gökmener (2016))

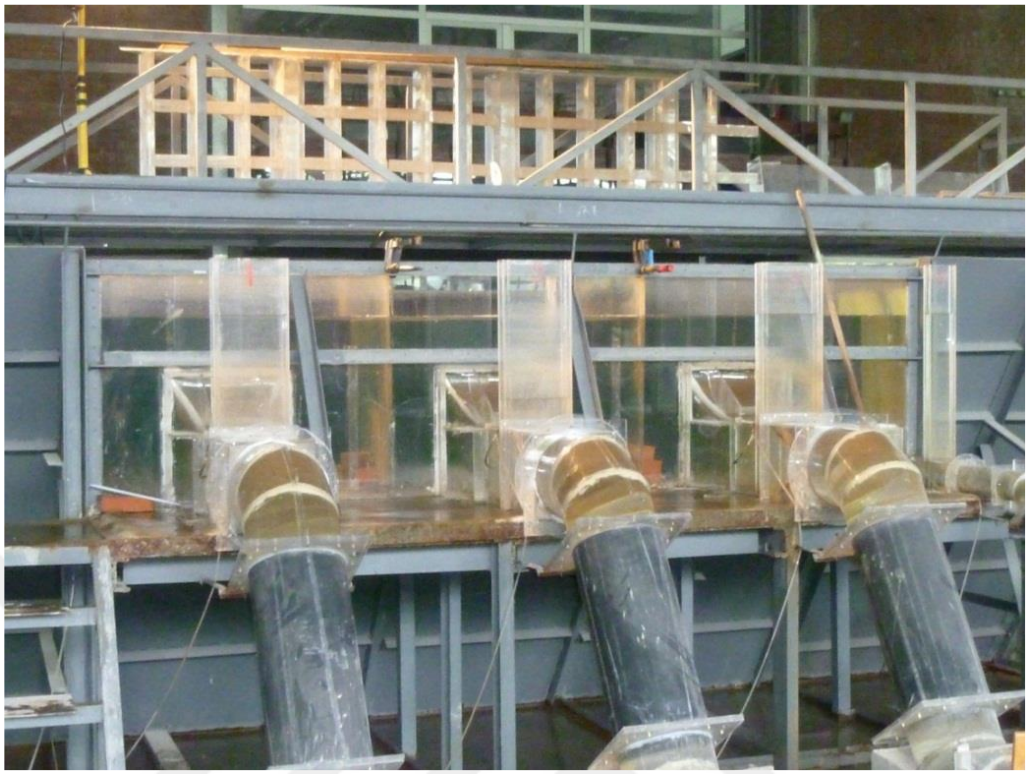

Figure 1.5 Close view of Gökmener's (2016) triple water intake structure model from dowstream (taken from Gökmener (2016))

CHAPTER 2

LITERATURE REVIEW

For several decades, researchers have undertaken experimental studies to establish reliable empirical formulas for the critical submergence depth of water intakes. However, in contemporary times, computational fluid dynamics (CFD) has become extensively utilized by researchers exploring vortex formation at the entrance of intake structures.

Anwar's (1967) experiments and theoretical research on the vortex prevention for different flow types show that strategic placement of floating rafts in locations where vortices occur can effectively prevent the formation of vortex.

Anwar's (1968) experiments and theoretical research on vortex formation and the vortex prevention for different flow types show that deep dimples and weak vortices are not associated with a radial Reynolds number higher than $1x10^3$.

Gordon (1970) examined the phenomenon of vortex formation at 29 different power plant intakes and derived empirical formulas for critical submergence depth, outlined as follows:

$$\frac{S_c}{D_i} = 1.70\ Fr \qquad 2.1$$

for symmetrical approach,

$$\frac{S_c}{D_i} = 2.27\ Fr \qquad 2.2$$

for asymmetrical approach flow conditions where S_c is the critical submergence depth which is the vertical separation between free water surface and highest point of the intake structure, D_i is the intake diameter and Fr is the Froude number.

Reddy and Pickford (1972) conducted flume experiments on horizontal intake structures with the aim of deriving accurate formulas for calculating critical submergence depth. In this study, Reynolds number and wavelength were disregarded due to the free surface flow nature of the experiments. The outcome of the research yielded two formulas, outlined as follows:

Configuration lacking vortex prevention devices;

$$S_c/D_i=Fr \tag{2.3}$$

Configuration with vortex prevention devices implemented;

$$S_c/D_i=1+Fr \tag{2.4}$$

Knauss (1987) examined the critical submergence depth of intake structures in hydroelectric power plants, establishing the minimum reservoir conditions necessary to prevent vortices, as depicted in Figure 2.1.

Yıldırım and Kocabaş (1995) conducted experimental investigation of the critical submergence depth of intakes. They utilized Rankine's half body, consisting of uniform channel flow and a point sink, to determine the critical submergence depth of a vertical intake. The study concluded with the derivation of a dimensionless formula for determining the critical submergence depth.

$$\frac{S_c}{D_i} = \frac{1}{2\sqrt{2}}\left(C_d \frac{V_i}{U_\infty}\right)^{1/2} \tag{2.5}$$

where C_d is the discharge coefficient of the intake, V_i is the velocity of intake pipe flow and U_∞ is the velocity of uniform approach channel flow.

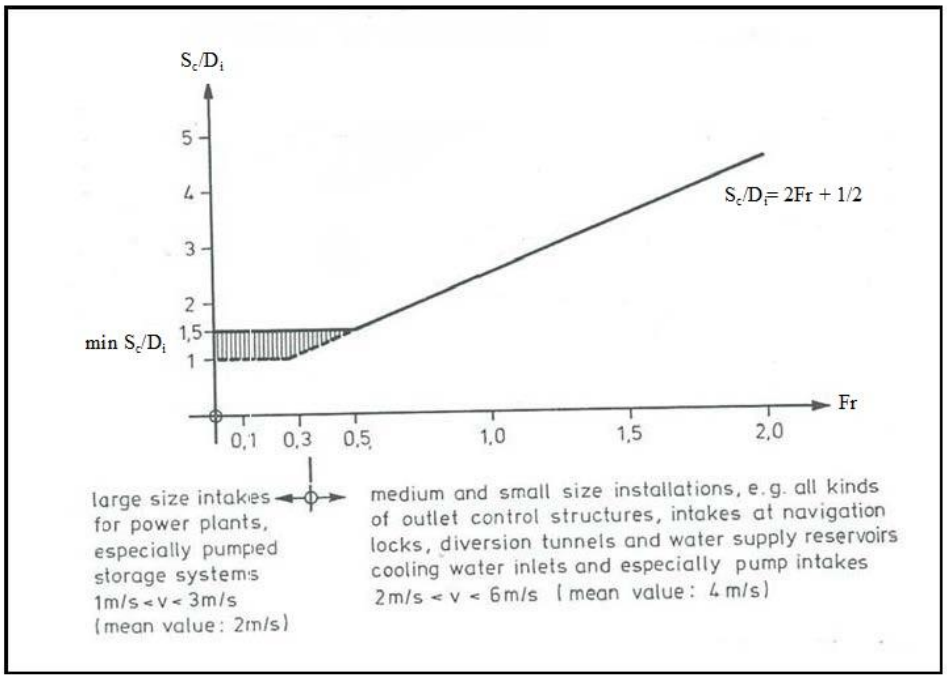

Figure 2.1 Recommended depth of submergence (Knauss, 1987)

Haspolat (2015) carried out experiments to explore the occurrence of air-entraining vortices under both symmetrical and asymmetrical approach flow conditions at horizontal intakes. Four horizontal intake pipes of varying diameters were employed, along with adjustable side walls to induce the desired symmetrical and asymmetrical approach flow conditions. A dimensionless equation for critical submergence was formulated, considering relevant geometric and hydraulic parameters. Through regression analysis, empirical equations were established to calculate the critical submergence depth, and these were then compared with similar equations found in the existing literature.

Göğüş, Köken and Baykara (2016) investigated the impact of hydraulic parameters on the generation of air-entraining vortices at horizontal intakes without induced circulation in the approach flow. The study utilized six horizontal intake pipes of varying diameters, and the experimental setup featured adjustable channel sidewalls. Experiments were conducted to determine critical

submergence depths under different discharge values and sidewall clearances. Empirical equations were derived to express the dimensionless critical submergence in terms of relevant dimensionless parameters. These equations demonstrated a high level of agreement with similar ones found in the existing literature.

Gürbüzdal (2009), Sarkardeh et. al (2010), Taştan and Yıldırım (2010) made experimental studies on the vortex formation, as well.

Numerical studies have also been undertaken to examine the formation of vortices and determine the critical submergence depth of water at intake structures.

Rosenhead (1931), approximated a vortex sheet by substituting the continuous distribution of vorticity with discrete point vortices. When investigating the impacts of a general disturbance, a singular wavelength was employed instead of considering all wavelengths. Numerical calculations were conducted using 2, 4, 8, and 12 vortices per wavelength. However, both Moore (1971) and Takami (1964) conducted experiments that demonstrated the instability of the point vortex method.

Chorin (1973) introduced the 3D vortex blob calculation, a vortex filament method. Instead of employing point vortices, Chorin utilized vorticity blobs to address the time-dependent Navier-Stokes equations, particularly for scenarios involving high Reynolds numbers. In this method, the center of the circle containing the velocity field was designated as the point vortex. This study marked a significant milestone in numerical vorticity calculations.

Hald and Del Prete (1978) provided a two-dimensional verification of Chorin's (1973) vortex blob method for the inviscid flow of incompressible fluid. The proof demonstrated the existence of a solution for short times, contingent on the condition that the vortex blobs overlaid each other. Subsequently, in 1979, Hald further proved the second-order convergence of the method for extended time periods.

Beale and Majda (1982a, 1982b) developed an alternative form of 3D vortex methods and demonstrated that these novel methods possess both high-order accuracy and stability. Furthermore, they established that the computational time for these vortex algorithms, based on Lagrangian stretching, is approximately equivalent to Chorin's (1973) algorithms.

Nagahara et al. (2003) made an experiment to measure the flow around vortex formation in a pump intake. They compared the velocity fields obtained from the experimental setup with those calculated through Computational Fluid Dynamics (CFD). Particle Image Velocimetry (PIV) was employed to observe the velocity fields in the experimental setup. The circulation values obtained from both CFD and PIV were approximately similar. However, the maximum velocity values from CFD calculations were smaller than the values observed experimentally. Additionally, the instantaneous maximum velocity values were larger than the time-averaged values, and the vortex core radii were smaller due to the unsteadiness of vortex formation. Consequently, the accuracy of CFD calculations was deemed unreliable, even with a sufficient grid distribution.

Okamura et al. (2007) performed numerical simulations of pump sumps using different Computational Fluid Dynamics (CFD) codes. The key findings of this investigation are summarized below:

- CFD codes demonstrated reliability in predicting vortex formation and its location visually.
- The critical submergence depths for both submerged vortex and air-entrained vortex were observed to be roughly proportional to the rate of flow.
- Although the velocity distribution at the intake mouth matched the experimental data, there were differences in vorticity strength and the distribution pattern of vorticity.

- The critical submergence depth was not solely determined by visible vortex formation; an additional process involving vortex core static pressure was necessary to determine the critical submergence depth.

Li et al. (2008) performed experiments to explore the formation of free surface vortices and compared the results with numerical simulations. Dye was used to trace the streamlines of the vortex structure, and Particle Image Velocimetry (PIV) was employed to measure the flow fields at different stages. The study concluded that the position and structure of the vortex core were consistent between the experimental and numerical models.

Nakayama and Hisasue (2010) performed a 3D numerical simulation of the intake reservoir of a small-scale hydropower facility using a Large Eddy Simulation (LES) solver. The simulation successfully captured the features of unsteady flow, vortex formation, and surface profiles, aligning well with the experimental model. Despite some differences in long-time simulation and experimental results, the simulation outputs were considered reliable.

Chen et al. (2012) compared the Volume of Fluid method with different turbulence models to determine the most suitable simulation method for vertical vortex formations. They investigated the effects of turbulent flow parameters on vertical vortex formation and concluded that the RNG k - ε model was more suitable than the k - ε model for simulating vertical vortices due to curved and immediately strained streamlines.

Zhao and Nohmi (2012) assessed the accuracy of the volume of fluid (VOF) method for free surface flows of pump intakes. Two cases were examined, and the VOF technique was found reliable for determining visible vortex structures for industrial use. However, discrepancies were noted between the VOF method and the fixed water surface method (FWSM) in the second case, attributed to boundary condition options at the water-air interface.

Sarkardeh et al. (2014) compared numerical and experimental results of flow movement in a reservoir in terms of vorticity. The study found good agreement between numerical simulation results and vorticity theories, with a close match between numerical and experimental results, except for a difference of about 10% in maximum velocity. A funnel-shaped flow was observed at the intake entrance, suggesting the need for finer grid resolution for a better understanding of flow movement.

Tataroğlu (2014) investigated vortex formation in an intake structure using Flow-3D, modeling the experimental studies of Baykara (2013). The critical submergence depths were determined, and the results of experimental and numerical studies were compared. Large Eddy Simulation (LES) results showed closer agreement with experimental results compared to laminar solutions, with the laminar solver failing to capture vorticity near walls resulting from turbulence. The study also examined the effects of anti-vortex plates and model scale.

CHAPTER 3

NUMERICAL MODELLING

3.1 Introduction

Numerical modelling of Gökmener's (2016) experimental setup is carried out by the Computational Fluid Dynamics (CFD) software named Flow-3D which is created by Flow Science, Inc. This software specializes in solving free surface flow problems by utilizing the Volume of Fluid (VOF) method.

The Volume of Fluid (VOF) method is employed in Flow-3D to address free surface flow problems by effectively tracking and locating the fluid-fluid interface. Although this method was recognized earlier, it was officially documented for the first time by Hirt & Nichols's (1981) study. The widespread adoption of this method gained momentum with advancements in computer technology.

Among the array of CFD software available, Flow-3D is chosen for this study for several reasons. Firstly, it stands out for its effectiveness in simulating free surface flows, employing an improved VOF algorithm known as TruVOF. Additionally, Flow-3D utilizes a non-body-fitted gridding technique, simplifying the grid generation process and making it more straightforward compared to any other CFD software which rely on body-fitted meshes.

3.2 Model Configuration

Software is organized into six submenus within the model main tab: general, fluids, physics, meshing & geometry, numeric and output. Following this sequence of menu tabs simplifies the modeling of any flow problem.

In the general submenu, crucial settings such as unit and version, interface tracking method, simulation finish time, number of fluids, flow mode are configured. All simulations use SI units, and the version option is set to double precision for enhanced accuracy. Either sharp interface or free surface is chosen as the interface tracking method. The finish time of the simulation is uniformly set to 50 seconds. Single-phase solution is applied to simulations. The fluid is assumed to be incompressible.

The fluid menu is dedicated to defining fluid properties.

Under the physics submenu, parameters like wall shear boundary conditions, gravity components, turbulence, and viscosity are entered. Wall shear boundary is chosen as no slip. The gravity component is entered to the z bar item as -9.81 m/s^2. Turbulence option is selected as Large Eddy Simulation (LES) and viscous flow is employed.

Moving to the meshing & geometry menu, members of the setup are created by the help of geometric shapes. Specifications of the members are assigned accordingly (see Figure 3.1). A rectangular solid component represents the intake structure, featuring a cylindrical hole member to represent the outflow pipe. The bottom of the channel is constituted of a rectangular solid prism. Mass source is constituted of a spherical solid member, symbolizing the inlet pipe in the experiment. The mass source's flow rate type is designated as volume flow rate. Starting discharge is given as 0 and increases to the full discharge within 5 seconds to avoid fluctuations in the free water surface in the approach channel.

Lastly, solid members act as impervious walls over the mass source to mitigate potential wave formations in the approach channel free water surface.

All members described above are depicted in Figure 3.1.

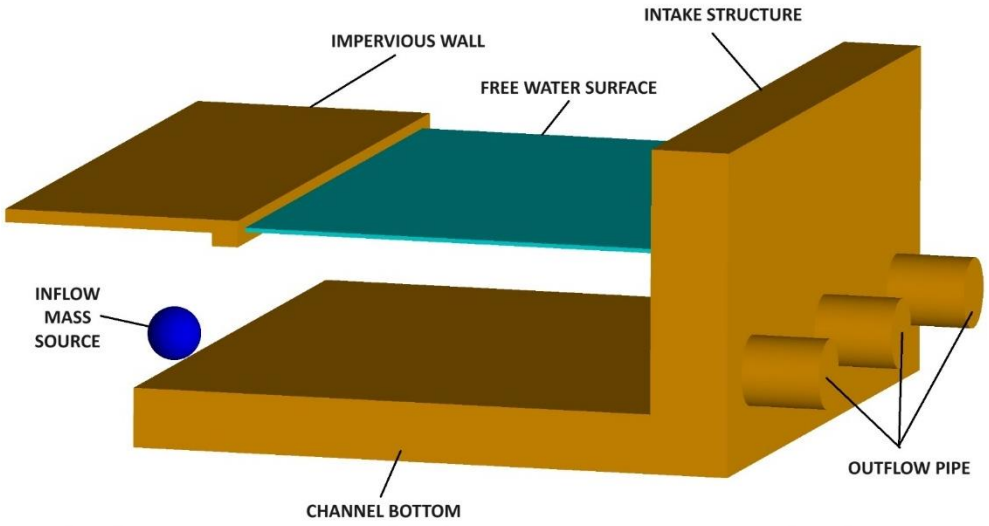

Figure 3.1 Model members

In each model, the geometry and flow specifications are configured based on the experimental cases conducted by Gökmener (2016). Outflow pipe diameter (D) is 26.50 cm and side wall distances (b) of the approach channel are 120.00 cm for each case. Given that the depths of critical submergence for different symmetrical cases are the focus of this study. Only remaining variable is the reservoir water depth, which is set for each case.

The process begins by setting the experiment setup water depth (h) where the vortex formation occurred as the starting depth of numerical setup. Subsequently, by incrementally adjusting the water depth (with a step size of 2.50 cm) and running the simulation again, the depth of critical submergence (Sc) is determined for each case. Single, double, and triple intake structures modeled in the simulations are given in Figure 3.2, Figure 3.3, and Figure 3.4.

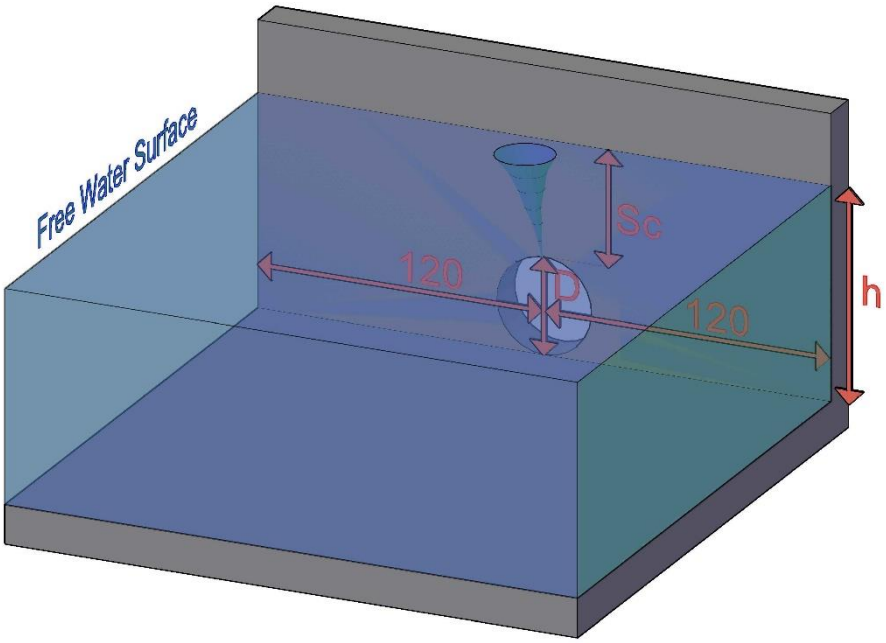

Figure 3.2 Single intake structure with dimensioning

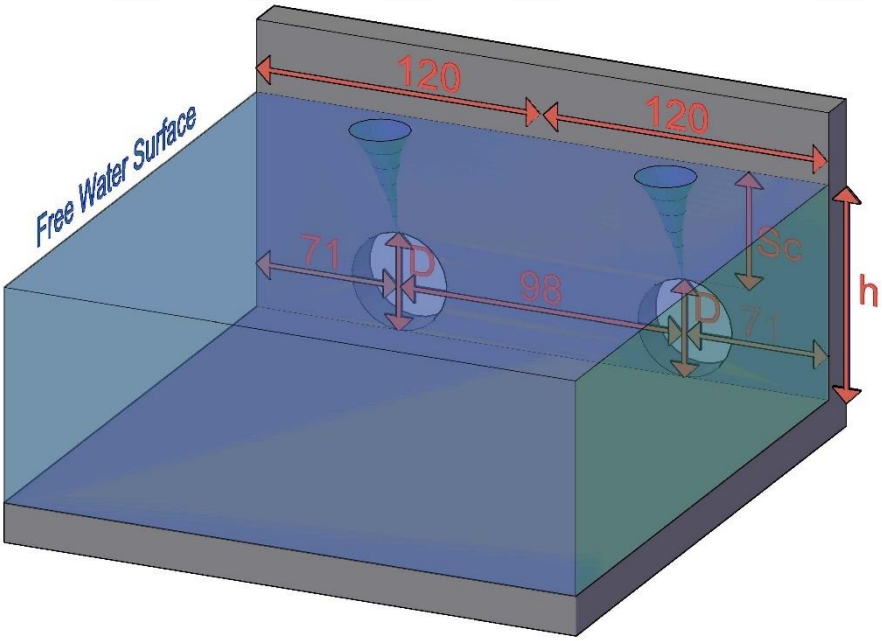

Figure 3.3 Double intake structure with dimensioning

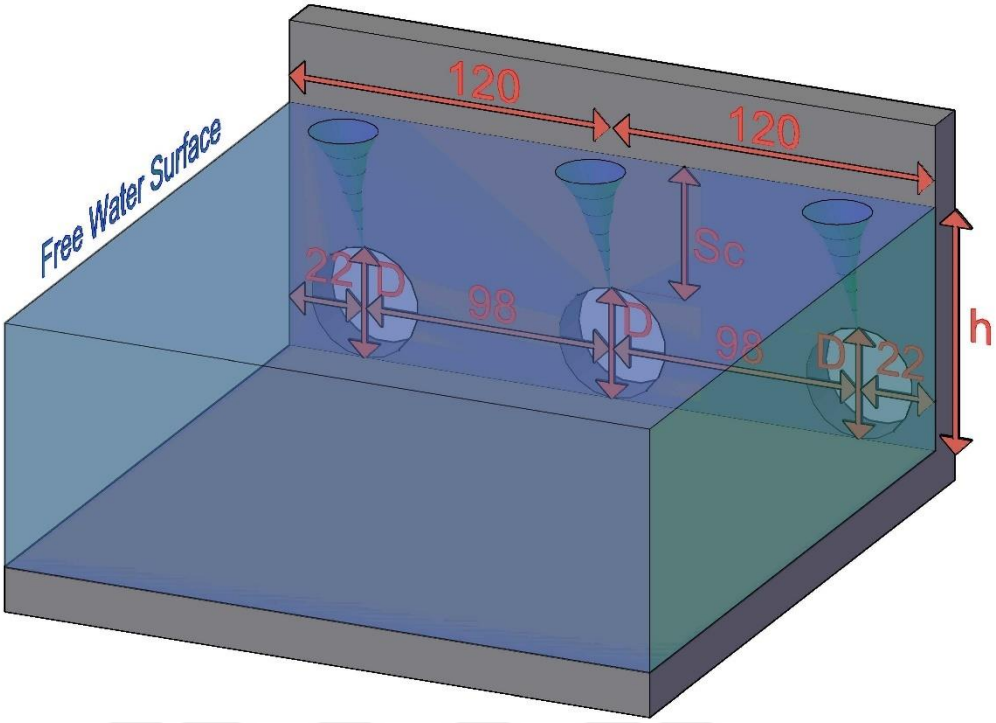

Figure 3.4 Triple intake structure with dimensioning

Upon modelling the case geometry, boundary conditions and meshing structure are designated under the meshing & geometry menu in the program. The software utilizes a technique named non-body-fitted gridding that decouples meshing from geometry construction. This allows for the alteration of either the grid or geometry without affecting the other. The chosen mesh system is rectangular and cartesian.

Selecting the size of the reservoir involves optimizing between accuracy and computational time. The volume of mesh size must be sufficiently big to assure the correctness of the model. Nevertheless, increasing volume of mesh results in increased computational time, which may be impracticable. This balance is crucial to strike an efficient compromise between computational resources and model accuracy.

Mesh block is designated as 4.00 m in length and 2.40 m in width. However, mesh block height varies in conjunction with the water depth. Mesh block height is chosen to be slightly greater than the depth of water to account for potential rises of the water level.

As previously stated, the selection of grid size is very important for balancing the accuracy and computational time of the model. For the initial attempt, an entire mesh block with a grid size of 0.02 m is chosen. However, for various depth of water values, vortex formation could not be seen, indicating the need for a smaller grid size. Yet, increasing the grid size for the entire block would result in impractical computational time.

To address this, a second finer mesh block is created with a grid size of 0.005 m, positioned near to intake since the vortex formation is anticipated to take place. This allows for the analysis of the vortex region with a finer mesh without significantly escalating the volume of mesh. Coarse and fine mesh blocks are illustrated in Figure 3.5.

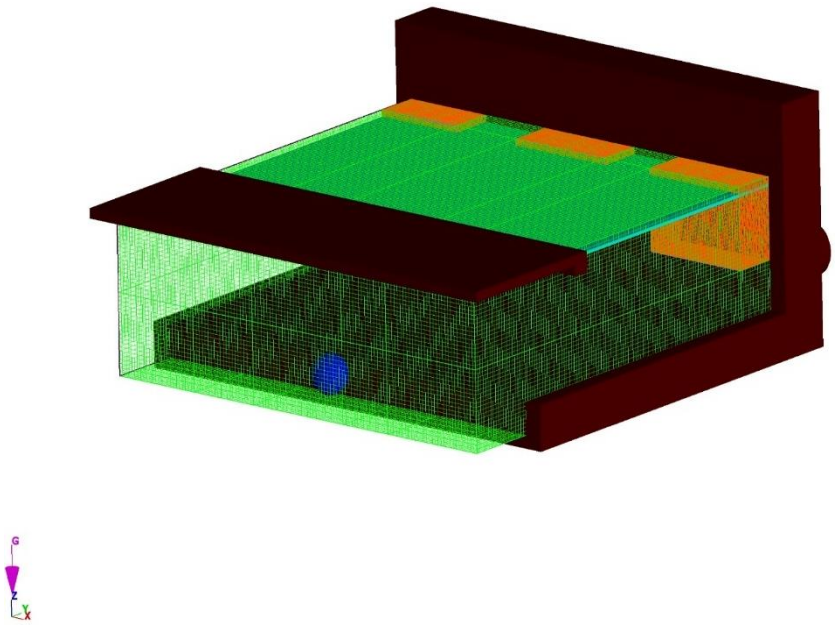

Figure 3.5 Coarse and fine mesh blocks

Lastly, mesh block boundary conditions are specified for each face. The top face of the coarse meshes is specified as symmetry (S), representing no flow through this face, and zero velocity perpendicular to it. Fine mesh block faces are designated as grid overlay (G), integrating the fine meshes into the coarse meshes. For the downstream face of the meshes, volume flow rate (Q) is given as the boundary condition. The bottom, side and upstream face of the coarse meshes are designated as wall (W), representing a no-slip boundary condition. Inflow of mass source and outflow discharge rates are the same, providing the desired flow conditions. Designated mesh block boundary conditions are illustrated in Figure 3.6.

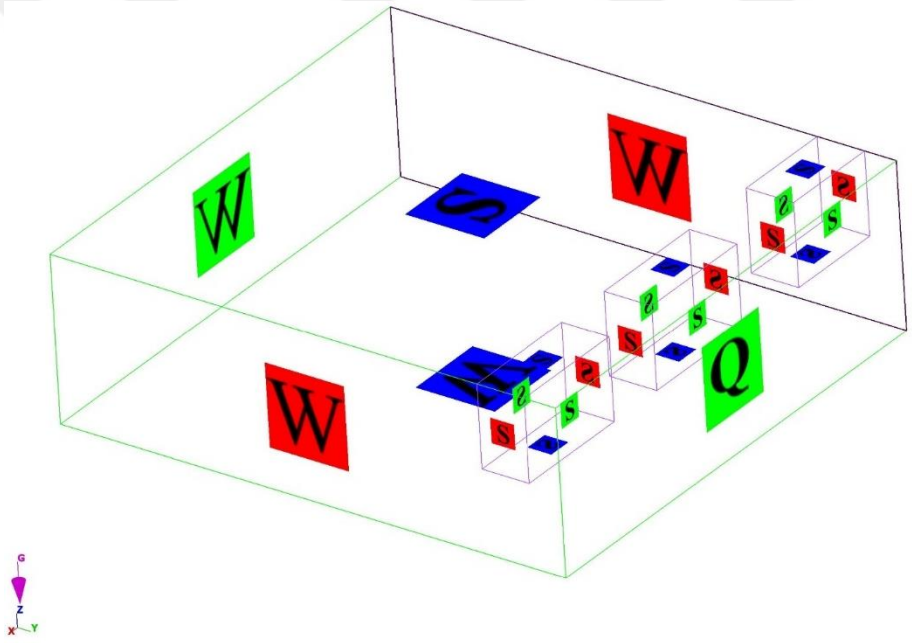

Figure 3.6 Boundary conditions

There are three main differences between experimental model of Gökmener (2016) and numerical models of this study. First one is the use of a spherical mass source in the numerical models while a direct flow from a 30 cm diameter inlet pipe was used in the physical experiments. Second difference is the use of solid members act as impervious walls over the mass source to mitigate potential

wave formations in the numerical models while a wall made of hollow bricks was used in the experimental study for the same purpose. Lastly, while the run time of the numerical simulations are 50 seconds, the observation time of the physical experiments were 15 – 20 minutes.

3.3 Simulation Procedure

This thesis investigates 12 different experimental cases from Gökmener (2016).

Initially, simulation is started with a water depth where the vortex formation is observed at the corresponding experimental case. Then, by the help of a tool of CFD post-processing, the results are examined for vortex formation. If vorticity is detected in the initial trial, depth of water is increased for the new simulation. This procedure is repeated until a scenario without the formation of vorticity is detected. Conversely, if no vortices are detected initially, depth of water is decreased for the new simulation, and it is run until detecting the formation of vorticity. Depth is adjusted in increments of 2.50 cm (Δh_s) during this process, leading to the determination of the critical submergence depth. In Figure 3.7, this procedure is tabulated as a flowchart.

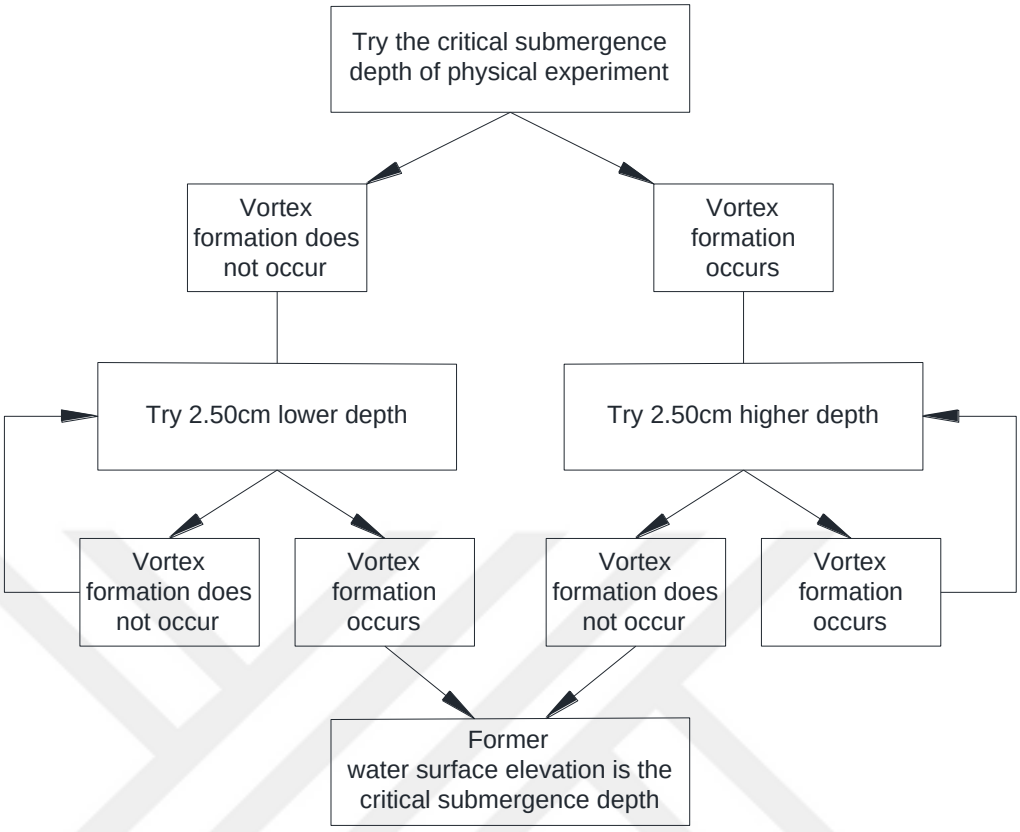

Figure 3.7 Simulation flowchart

The time of computation for these simulations is crucial for practicality. Determining the depth of critical submergence (Sc) of a case typically requires approximately 5 to 6 simulation runs. Given that the time of computation for a single simulation is around 30 hours on a workstation with the specifications given in Table 3.1, the time to solve one case is approximately one week, encompassing both simulations and analyses, provided there are no other issues related with software or internet connection. As a result, the total computational time for the entire study is approximately 2,880 hours, equivalent to 120 days.

Table 3.1 PC specifications

Model:	Dell Precision T7600
Processors:	2x Intel® Xeon™ E5-2650 2.00GHz Eight (8) Core 20MB
Operating System:	Windows 10 (64-bit)
Memory:	128GB (16x 8GB) PC3-12800R Memory
Graphics Card:	2 GB Nvidia Quadro 4000
Raid Controller:	Dell Perc H310

In Table 3.2, study cases parameters are given.

Table 3.2 Simulations

Intake #	Case #	D (cm)	b (cm)	Q (lt/s)
Single Intake	01	26.50	120.00	165.00
	02	26.50	120.00	150.00
	03	26.50	120.00	135.00
	04	26.50	120.00	123.61
	05	26.50	120.00	110.14
Double Intake	06	26.50	120.00	122.69
	07	26.50	120.00	110.04
	08	26.50	120.00	96.79
	09	26.50	120.00	88.21
	10	26.50	120.00	75.08
Triple Intake	11	26.50	120.00	135.00
	12	26.50	120.00	122.69
	13	26.50	120.00	110.04
	14	26.50	120.00	96.79
	15	26.50	120.00	87.96

3.4 Viscous Solver

Type of the flow is identified as viscous, accompanied by no-slip condition at the boundaries. Second order momentum equations is used to effectively capture the dynamics of swirling flows.

In a study conducted by Tataroğlu (2014) on the phenomenon of vortex formation at horizontal intakes, an evaluation was performed comparing the Reynolds Averaged Navier-Stokes (RANS) model with the Large Eddy Simulation (LES) turbulence model. Similar to the methodology employed in our study, Flow-3D was utilized for simulations. The results suggested that when RANS model and LES turbulence model are compared, latter exhibited greater accuracy and closer conformity to experimental observations. Tataroğlu further suggested that the LES turbulence model is more adequate at showing vorticity in close proximity to the surfaces.

Therefore, the LES turbulence model is employed in the simulations. Similarity theory of turbulence suggested by Kolmogorov (1941) which is treating small and large scales separately is the basis of the LES turbulence model. The larger eddies are straightforwardly analyzed, while the influence of smaller eddies is parameterized through the use of a sub-grid-scale model (SGS). This approach allows for the implicit consideration of the unresolved small-scale fluid movement's effect.

3.5 Grid Size Dependency

Optimizing grid size is crucial for achieving cost-effective simulations without compromising accuracy. In order to assess grid size dependency, various grid sizes are applied to the same model in a selected test case. Two simulations were tried to conduct, with one of them being 50% coarser. Based on this comparison, the optimal grid size is determined for the remaining cases.

Case 5 is selected for test since this case has the smallest grid size. It is composed of a single intake with 26.50 cm outflow pipe, 110.14 l/s discharge and 67.50 cm free water surface elevation. Side clearances of the setup are 120 cm symmetrically. Table 3.3 presents the run time and grid size of the test case.

Table 3.3 Grid size dependency comparison

	Coarse Grid Size (m)	Fine Grid Size (m)	Number of Grid Points (Fine Mesh)	Number of Grid Points (Coarse Mesh)	Total Number of Grid Points	Run Time (hours:minutes)
Case-05 - opt.1	0.010	0.002	5,406,720	4,800,000	10,206,720	358:49
Case-05 - opt.2	0.020	0.004	600,000	684,000	1,284,000	21:16

Even though, the case with the smallest grid size among all cases was selected computational run time of the simulation with the smaller grid sizes makes it impossible to investigate all 15 cases. So, the preference is for the coarser mesh option with 0.004 m fine and 0.020 m coarse grid sizes in the remaining simulations as detailed in the Model Configuration section.

CHAPTER 4

RESULTS OF ANALYSES

4.1 Introduction

In result of analyses, a comparison is made between the experimental findings and numerical results to assess their accuracy. Results of analyses are displayed at Appendix A, containing cross sections of ribbon streamlines and contours of vorticity from various zones.

Depth of critical submergence is identified by increasing or decreasing the water depths 2.50 cm, denoted by the symbol 'Δh_s'. This implies that there is a possibility of occurring another vortex formation between the water depths arranged by an increment of 2.50 cm. In essence, the margin of error for these numerical simulations is +2.49 cm.

The vortex forming at the free surface is big enough to be observed however, it gets smaller in the direction of intake mouth. For this problem, opting for a finer mesh can aid in observing a larger section of the air-core. Yet, employing a finer mesh size entails an impractical and costly solution. Therefore, vorticity contours and values of circulation is taken into consideration to determine whether a full air-core vortex is reaching the intake.

4.2 Analysis

In order to see the 'Scale Effect,' a prototype study was planned, but it couldn't be executed due to its high cost and infeasibility. Even with these limited number of meshes, each simulation takes an average of 30 hours. In addition, for each case, at least 4-5 simulations are need to be conducted with a 2.50 cm increment.

The prototype model created for Case-5 was run, but the expected run time was almost 15 days, making it impractical to be solved with the available computational power.

4.3 Comparison of Physical Experiments and Numerical Simulation Results

This study intents to observe the conformity of numerical simulations with the physical experiments in the aspect of analysis of vortex formation at horizontal symmetrical intake structures.

In Table 4.1, water depths (h), depths of the critical submergence (Sc) and values of circulation (Γ) from both experimental analysis and corresponding simulations are presented.

$$\Gamma = \iint \omega z \, . \, dA$$

where dA is the per-unit area taken around a confined infinitesimal loop and ωz represents vertical vorticity. Circulation values are derived by performing integration of vertical vorticity values over the confined vortex core area.

Within the vortex core, circulation values are computed for free water surface level and given as (Γa), for slightly beneath the observable vortex core and given as (Γb), and for mid-level of critical submergence depth and given as (Γc) in Table 4.1. These values exhibit consistency which implies that the circulation value remains relatively constant from the top of the intake mouth to the free water surface. For example, for Case-01 Figures A1, A2 and A3 give the vertical vorticity contours on horizontal planes at the free surface, beneath the observable vortex core and at mid-level of critical submergence depth, respectively. In these figures the red patch of high vorticity represents the air core vortex. Circulation values discussed above are obtained by isolating this red patch and integrating the vertical vorticity over this patch. For Case-01, 3D streamlines and isosurface of the air water interface is shown in the longitudinal and transversal directions

in Figures A4 and A5 respectively. One can clearly identify the air-core vortices starting from the free surface down to the intake entrance from the streamline patterns. For all the cases tested similar figures are plotted and given in Appendix-A.

Table 4.1 Experimental and numerical simulation results

						Physical Exp.		Numerical Simulation					
Intake #	**Case #**	**D (cm)**	**b (cm)**	**Q (lt/s)**	**Fr**	**S_c (cm)**	**S_c/D**	**S_c (cm)**	**S_c* (cm)**	**S_c/D**	**Γ a**	**Γ b**	**Γ c**
Single Intake	01	26.50	120.00	165.00	1.86	-	-	66.00	79.25	2.49	2.94E-02	3.81E-02	3.15E-02
	02	26.50	120.00	150.00	1.69	-	-	61.00	74.25	2.30	2.38E-02	5.89E-02	6.44E-02
	03	26.50	120.00	135.00	1.52	-	-	58.50	71.75	2.21	1.68E-02	1.91E-02	3.19E-02
	04	26.50	120.00	123.61	1.39	52.20	1.97	41.00	54.25	1.55	-1.38E-02	-3.39E-02	-4.61E-02
	05	26.50	120.00	110.14	1.24	50.80	1.92	41.00	54.25	1.55	3.81E-02	2.44E-02	2.64E-02
Double Intake	06	26.50	120.00	122.69	1.38	47.50	1.79	33.50	46.75	1.26	2.24E-02	3.46E-02	4.22E-02
	07	26.50	120.00	110.04	1.24	46.20	1.74	28.50		1.08	1.55E-02	5.12E-02	5.49E-02
	08	26.50	120.00	96.79	1.09	44.00	1.66	23.50		0.89	1.09E-02	2.22E-02	2.68E-02
	09	26.50	120.00	88.21	0.99	42.30	1.60	21.00		0.79	-2.91E-02	-3.68E-02	-4.08E-02
	10	26.50	120.00	75.08	0.84	39.40	1.49	16.00		0.60	-8.28E-03	-1.04E-02	-1.06E-02
Triple Intake	11	26.50	120.00	135.00	1.52	-	-	38.50		1.45	1.09E-02	1.80E-02	2.99E-02
	12	26.50	120.00	122.69	1.38	-	-	36.00		1.36	-1.29E-02	-3.63E-02	-3.03E-02
	13	26.50	120.00	110.04	1.24	-	-	31.00		1.17	-1.93E-02	-2.25E-02	-2.94E-02
	14	26.50	120.00	96.79	1.09	-	-	23.50		0.89	-2.24E-02	-2.51E-02	-2.30E-02
	15	26.50	120.00	87.96	0.99	48.50	1.83	23.50		0.89	-5.74E-03	-1.41E-02	-1.20E-02
	16	26.50	120.00	76.57	0.86	47.10	1.78	-		-	-	-	-
	17	26.50	120.00	67.06	0.75	41.00	1.55	-		-	-	-	-
	18	26.50	120.00	59.35	0.67	36.80	1.39	-		-	-	-	-

When numerical simulation and physical experiment results are compared it is seen that numerical simulations give smaller critical submergence depth values than the observed ones in the physical experiments. Also, it is noted that as the discharge decreases the difference between the physical experiments and the numerical simulations increases. In Figure 4.1 results are given for all setups with available results of both numerical and physical experiments.

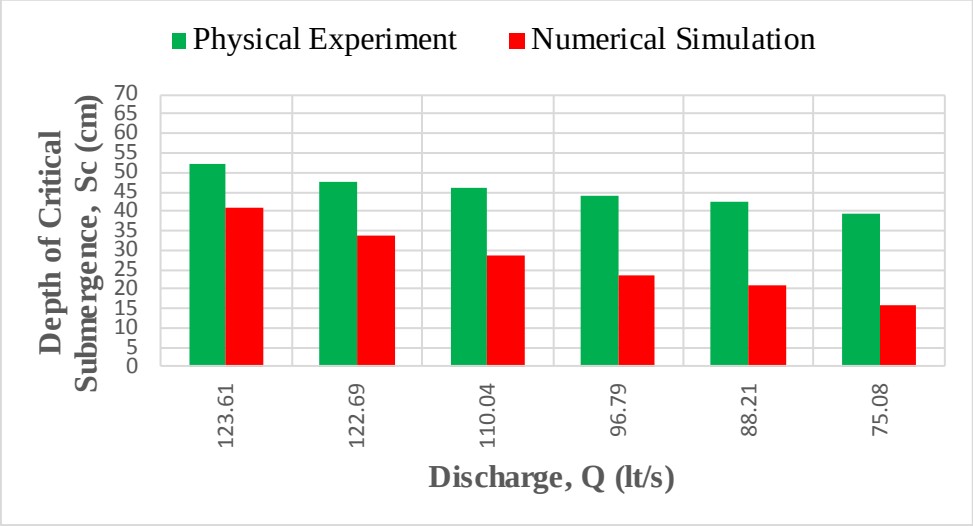

Figure 4.1 Depth of critical submergence and discharge values for all setups with available results of both numerical and physical experiments

The discrepancy of numerical simulations and physical experiments is shown in Table 4.2. For the single intakes the difference between the experimental and numerical results are within a range of 14-21%, whereas this difference is 24-59% for double intakes and the same difference is 46-52% for the triple intakes. It is important to note that there is only one common triple intake case compared with the experiment.

Table 4.2 Numerical simulation discrepancy margins

			Physical Experiment	**Numerical Simulation**	**Max. Discrepancy Percentage (%)**	**Min. Discrepancy Percentage (%)**
Intake #	**Case #**	**Q (lt/s)**	**S_c (cm)**	**S_c (cm)**		
Single Intake	04	123.61	52.20	41.00	21.46	16.67
	05	110.14	50.80	41.00	19.29	14.37
Double Intake	06	122.69	47.50	33.50	29.47	24.21
	07	110.04	46.20	28.50	38.31	32.90
	08	96.79	44.00	23.50	46.59	40.91
	09	88.21	42.30	21.00	50.35	44.44
	10	75.08	39.40	16.00	59.39	53.05
Triple Intake	15	87.96	48.50	23.50	51.55	46.39

4.4 Comparison of Critical Submergence and Number of Intakes

There are two specific discharges in the data set (110 lt/s and 123 lt/s) where there are both experimental and numerical data for single (cases 4 and 5) and double (cases 6 and 7) intakes. It would be interesting to make a comparison for these two discharges. Comparison of experimental and numerical critical submergence depths for these two discharges are given in Figure 4.3. Both in the numerical simulations and the experimental results, there exist a correlation between critical submergence and the number of intakes. As the number of intakes increase for a given discharge value, critical submergence value decreases. Correlations between these values are given in Figure 4.3 for the discharge values of 110 lt/s (cases 5 and 7) and 123 lt/s (cases 4 and 6).

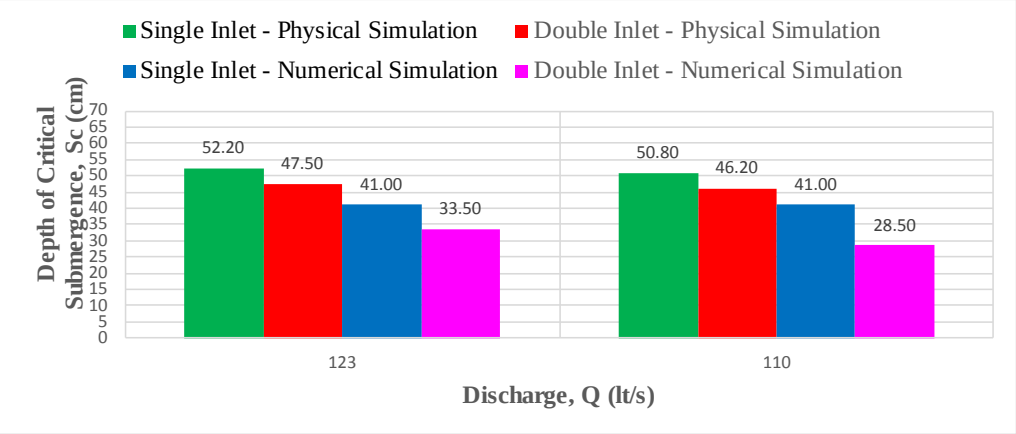

Figure 4.2 Depth of critical submergence and number of intake values of physical experiment and numerical simulation results for given discharge values

4.5 Comparison of Critical Submergence and Discharge

In the numerical simulation and experiment results, there exist a correlation between critical submergence and discharge values. However, up to this point the discharge values defined were the total discharge passing through all the

intakes. In order to make a direct comparison with the single intake discharge passing through each intake is calculated and presented for the double and triple intakes in Figure 4.2. Change in critical submergence depth with the discharge passing through one intake is presented in Figure 4.2. Both experimental and numerical results are presented here. It can be observed that as the discharge increases for a given setup, critical submergence depth also increases for both physical experiments and numerical simulations. Consistently in all the simulations and experiments critical submergence depth increases with the increase in discharge. One important observation here is related to the behavior of double and triple intakes at similar discharges. It can be seen that both for the experiments and numerical simulations triple intakes give larger critical submergence depths compared to double intakes. For the single intakes there is an abrupt change in the critical submergence depth around the discharge of 130 lt/s.

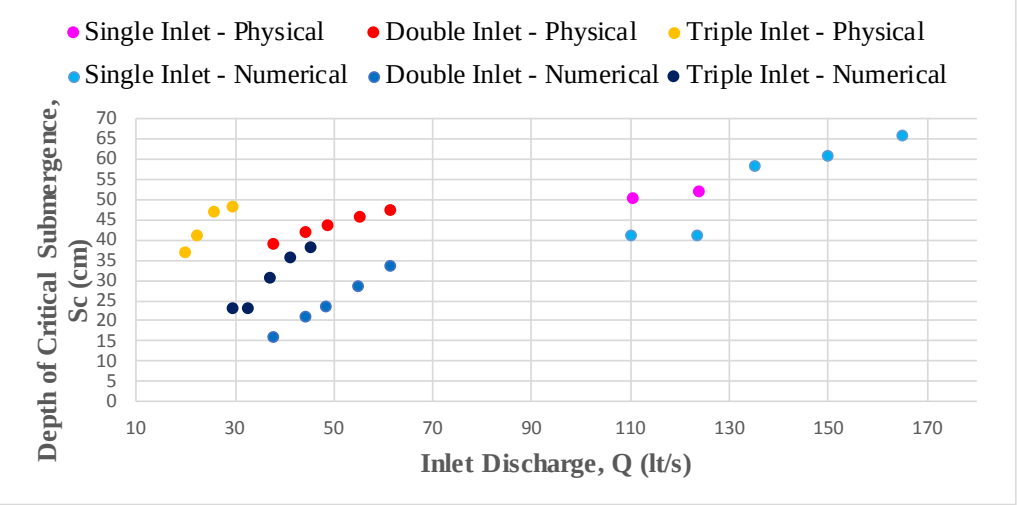

Figure 4.3 Depth of critical submergence and discharge values of physical experiment and numerical simulation results

4.6 Location of the Air Core Vortex

The location of the air-core vortex is investigated for all the simulations conducted. For the single intake simulations air-core vortex is always observed close to the center of the intake pipe. It should be noted that there were some small dimples forming at different locations within the reservoir however air-core vortices were always forming at the center. For the double intakes the location where the air-core vortex forms slightly shifted from the centerline of the intake towards the other intake. For the triple intakes, air core vortex forming at the side intakes seem to shift towards the sidewalls or at least streamlines which create the vortex are started to form from sidewalls and moved towards to center of corresponding intake. The locations of vortex formations for all simulations could be seen in the figures given in Appendix-A.

CHAPTER 5

CONCLUSIONS

In the current investigation, the experimental study conducted by Gökmener (2016) were modeled numerically and simulated using Flow 3D to explore vortex formation at symmetrical intakes. The depth of critical submergence obtained from both numerical and experimental results are used to compare the conformity of the numerical CFD simulations with the experimental study. The Large Eddy Simulation (LES) model was employed for this study. Approximately 85 simulations are performed for 15 cases within the scope of this study. Conclusions drawn from this study are:

1. It is not possible to visualize the full length of the air-core vortex with the numerical simulations as the core of the vortex becomes so small in the direction of the intake mouth and a very fine grid resolution is required to resolve the vortex. However, circulation values along the path of the vortex can be used to identify the presence of the air-core vortex. As this value remains almost constant along its path.

2. For the simulations, an increment of 2.50 cm for the water depth was utilized. This resulted in a discrepancy for critical submergence depth within the range of 14% - 59%. To mitigate this discrepancy, one potential solution is reducing the grid size. However, this adjustment would come at the expense of increased computation time.

3. All the numerical simulations under-estimates the critical submergence depth. Although, there is an under estimation in the critical submergence depth, numerical simulations catch the correct increasing trend in critical submergence depth with increased discharge similar to the experimental results.

4. While physical experiments had an observation time of around 15- 20 minutes (Gökmener, 2016, p. 34), the present simulations are run for only 50 seconds due to long simulation run times. More conformity with experimental results could be achieved with longer simulation period. However, it will not be practical to do this as the run time for one simulation will increase approximately from 30 hours to 600 hours.

5. For similar intake discharges triple intakes have larger critical submergence depth compared to the double intakes.

6. For a constant total discharge, as the number of intake units increases critical submergence depth increase. Obtaining higher critical submergence depths as the number of intakes increases show that sidewalls and other intakes further promote the formation of these vortices.

For future research endeavors, numerical simulations can be expanded beyond the scope of experimental investigations with the help of Flow 3D software.

REFERENCES

Anwar, H.O. (1968), "Prevention of Vortices at Intakes", Water Power 1968(10), 393-401.

Baykara, A. (2013), "Effect of Hydraulic Parameters on the Formation of Vortices at Intake Structures", M.Sc. Thesis, Civil Engineering Dept., Middle East Technical University.

Beale, J.T. and Majda, A. (1982a), "Vortex methods I: Convergence in Three Dimensions", Mathematics of Computation, Vol. 39, No. 159, 1-27.

Beale, J.T. and Majda, A. (1982b), "Vortex methods II: Higher Order Accuracy in Two and Three Dimensions", Mathematics of Computation, Vol. 39, No. 159, 29-52.

Chen, Y., Wu, C., Wang, B. and Du, M. (2012), "Three-dimensional Numerical Simulation of Vertical Vortex at Hydraulic Intake", 2012 International Conference on Modern Hydraulic Engineering, March 9-11, Nanjing, Jiangsu Province, China.

Chorin, A.J. (1973), "Numerical Study of Slightly Viscous Flow", Journal of Fluid Mechanics, 57, 785-796.

Chorin, A.J. (1982), "The Evolution of a Turbulent Vortex", Communications in Mathematical Physics, 83, 517-535.

Durgin, W.W. and Hecker, G.E. (1978), the Modeling of Vortices in Intake Structures. Proc IAHR-ASME-ASCE Joint Symposium on Design and Operation of Fluid Machinery, CSU Fort Collins, June 1978 vols I and III.

Flow Science Inc., www.flow3d.com, last visited on August 2017.

Gordon, J.L. (1970), “Vortices at Intakes”, Water Power 1970(4), 137-138.

Göğüş, M., Köken M., Baykara A. (2016), “Formation of Air-entraining Vortices at Horizontal Intakes without approach flow induced circulation”, Journal of Hydrodynamics, Vol. 28, Iss. 1, 102-113.

Gürbüzdal, F. (2009), “Scale Effects on the Formation of Vortices at Intake Structures”, M.Sc. Thesis, Civil Engineering Dept., Middle East Technical University.

Hald, O. (1979), “Convergence of Vortex Methods for Euler’s Equations. II”, SIAM Journal on Numerical Analysis, Vol. 16, No. 5, 726-755.

Hald, O. and Del Prete V.M. (1978), “Convergence of Vortex Methods for Euler’s Equations”, Mathematics of Computation, Vol. 32, No. 143, 791-809.

Haspolat, E. (2015), “Determination of Critical Submergence Depth at Horizontal Intakes”, M.Sc. Thesis, Civil Engineering Dept., Middle East Technical University.

Hirt, C.W., Nichols, B.D. (1981), “Volume of Fluid (VOF) Method for the Dynamics of Free Boundaries”, Journal of Computational Physics, Vol. 39, Iss. 1, 201-225.

Knauss, J. (1987), “Swirling Flow Problems at Intakes”, A.A. Balkema, Rotterdam.

Kolmogorov, A. (1941), “The Local Structure of Turbulence in Incompressible Viscous Fluid for Very Large Reynolds’ Numbers”, Doklady Akademiia Nauk SSSR, Vol.30, 301-305.

Li, H., Chen, H., Ma, Z. and Zhou, Y. (2008), “Experimental and Numerical Investigation of Free Surface Vortex”, Journal of Hydrodynamics, 20(4), 485-491.

Moore, D.W. (1971), “The Discrete Vortex Approximation of a Finite Vortex Sheet”, California Inst. Of Tech. Report AFOSR-1804-69.

Nagahara, T., Sato, T., Okamura, T., Iwano, R. (2003), “Measurement of the Flow around the Submerged Vortex Cavitation in a Pump Intake by Means of PIV”, Fifth International Symposium on Cavitation (cav2003), Osaka, Japan, November 1-4.

Nakayama, A. and Hisasue, N. (2010), “Large Eddy Simulation of Vortex Flow in Intake Channel of Hydropower Facility”, Journal of Hydraulic Research, Vol.48, Iss. 4., 415-427.

Okamura, T., Kyoji, K. and Jun, M. (2007), “CFD Prediction and Model Experiment on Suction Vortices in Pump Sump”, The 9th Asian International Conference on Fluid Machinery, October 16-19, Jeju, Korea.

Reddy, Y.R. and Pickford, J.A. (1972), “Vortices at Intakes in Conventional Sumps”, Water Power 1972(3), 108-109.

Rosenhead, L. (1931), “The Formation of Vortices from a Surface of Discontinuity”, Proc. Roy. Soc. London Series A, Containing Papers of a Mathematical and Physical Character, Vol. 134, Iss. 823, 170-192.

Sarkardeh, H., Zarrati, A.R., Jabbari, E. and Marosi, M. (2014), “Numerical Simulations and Analysis of Flow in a Resorvoir in the Presence of Vortex”, Engineering Applications of Computational Fluid Mechanics, Vol. 8, Iss. 4, 598-608.

Sarkardeh, H., Zarrati, A.R., Roshan, R. (2010), “Effect of Intake Head Wall and Trash Rack on Vortices”, Journal of Hydraulic Research, Vol. 48, Iss. 1, 108-112.

Takami, H. (1964), “Numerical Experiment with Discrete Vortex Approximation, with Reference to the Rolling Up of a Vortex Sheet”, Dept. of Aero. and Astro., Stanford University Report SUDAER 202.

Tataroğlu, R.M. (2014), “Numerical Investigation of Vortex Formation at Intake Structures Using Flow 3D Software”, M.Sc. Thesis, Civil Engineering Dept., Middle East Technical University.

Taştan, K. and Yıldırım, N. (2010), “Effects of Dimensionless Parameters on Air-entraining Vortices”, Journal of Hydraulic Research, Vol. 48, Iss. 1, 57-64.

Yıldırım, N. and Kocabaş, F. (1995), “Critical Submergence for Intakes in Open Channel Flow”, Journal of Hydraulic Engineering, ASCE, Vol. 121, Iss. 12, 900-905.

Zhao, L.J. and Nohmi, M. (2012), “Numerical Simulation of Free Water Surface in Pump Intake”, IOP Conference Series: Earth and Environmental Science, Vol. 15, Part 5.

APPENDICES

A. NUMERICAL SIMULATION RESULTS

Case-01: Single Intake with D = 26.50 cm, b = 120.00 cm, Q = 165.00 l/s, free water elevation = 92.50 cm

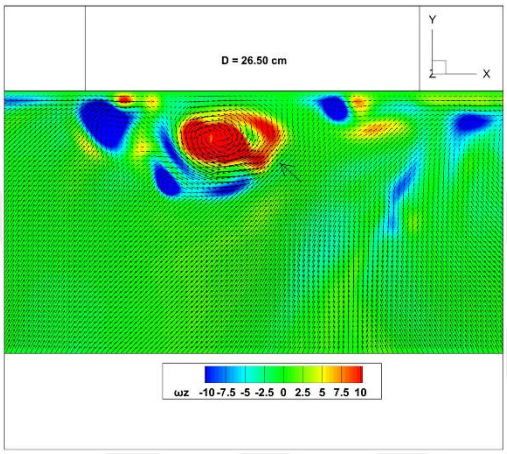

Figure A.1 Case-01 z-axis vorticity (ωz, 1/sec) at the free water surface

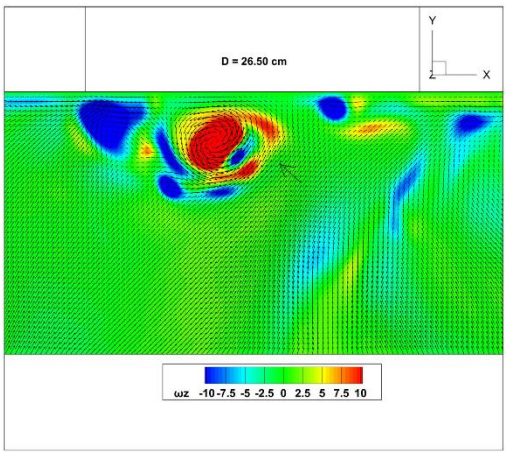

Figure A.2 Case-01 z-axis vorticity (ωz, 1/sec) slightly beneath the observable vortex core

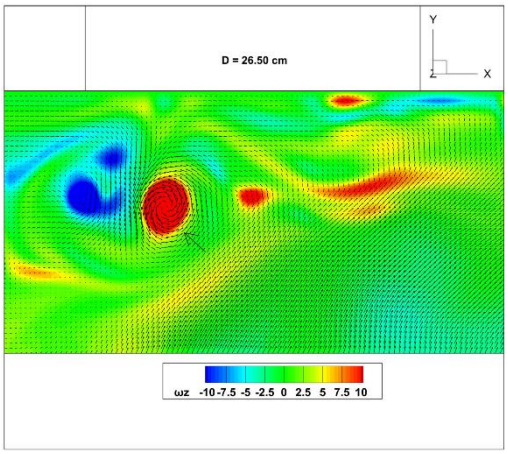

Figure A.3 Case-01 z-axis vorticity (ωz, 1/sec) at mid-S_c level (59.50 cm)

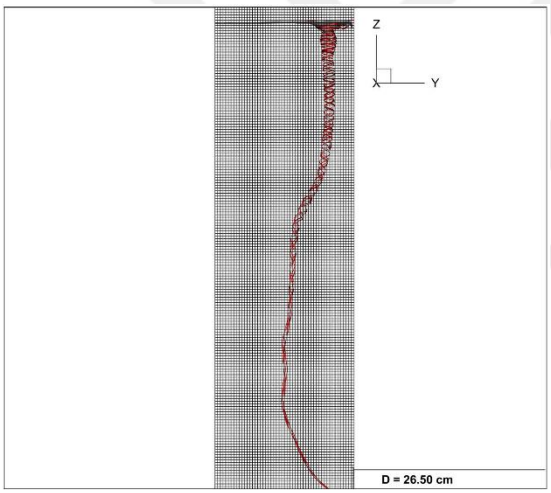

Figure A.4 Case-01 3D streamlines and isosurfaces of the air-water interface cross-section (longitudinal (y) direction)

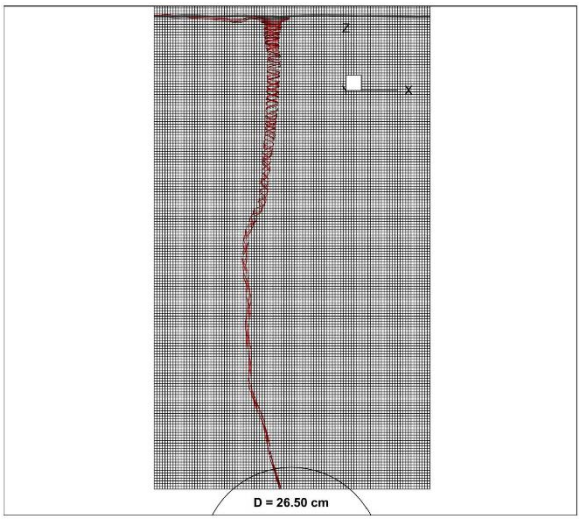

Figure A.5 Case-01 3D streamlines and isosurfaces of the air-water interface cross-section (transverse (x) direction)

Case-02: Single Intake with D = 26.50 cm, b = 120.00 cm, Q = 150.00 l/s, free water elevation = 87.50 cm

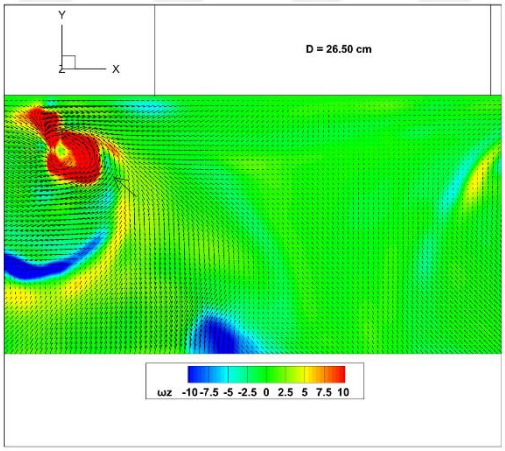

Figure A.6 Case-02 z-axis vorticity (ωz, 1/sec) at the free water surface

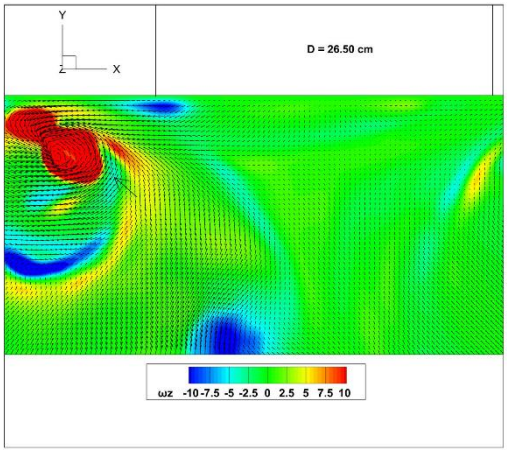

Figure A.7 Case-02 z-axis vorticity (ωz, 1/sec) slightly beneath the observable vortex core

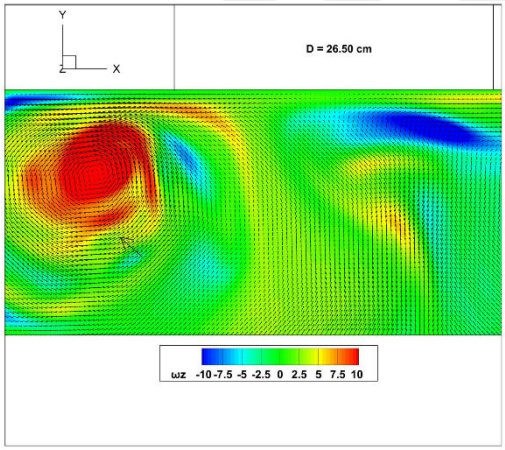

Figure A.8 Case-02 z-axis vorticity (ωz, 1/sec) at mid-S_c level (57.00 cm)

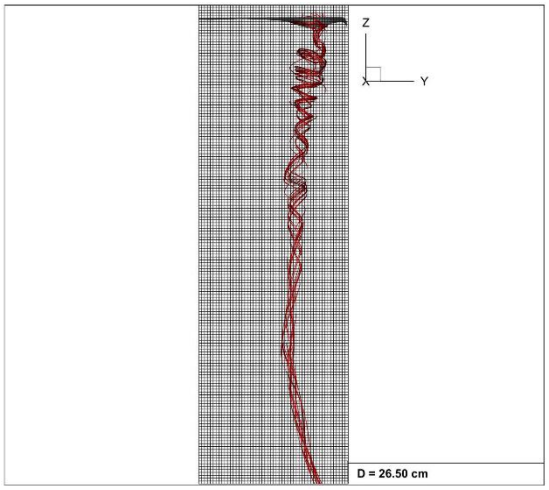

Figure A.9 Case-02 3D streamlines and isosurfaces of the air-water interface cross-section (longitudinal (y) direction)

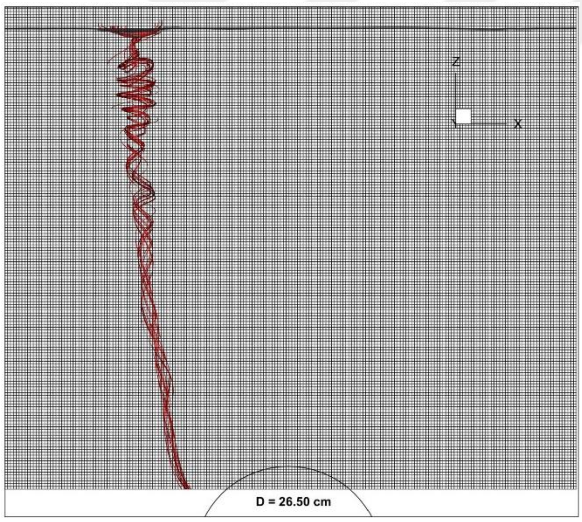

Figure A.10 Case-02 3D streamlines and isosurfaces of the air-water interface cross-section (transverse (x) direction)

Case-03: Single Intake with D = 26.50 cm, b = 120.00 cm,

Q = 135.00 l/s, free water elevation = 85.00 cm

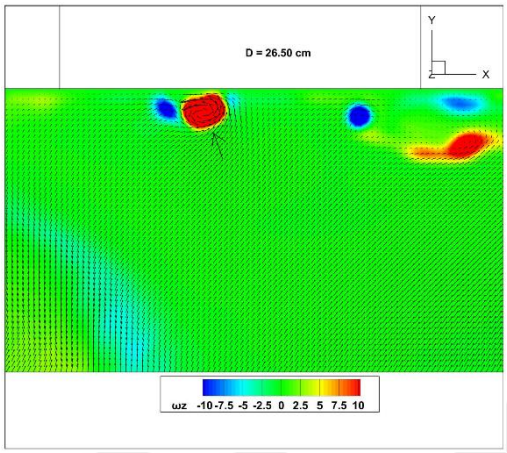

Figure A.11 Case-03 z-axis vorticity (ωz, 1/sec) at the free water surface

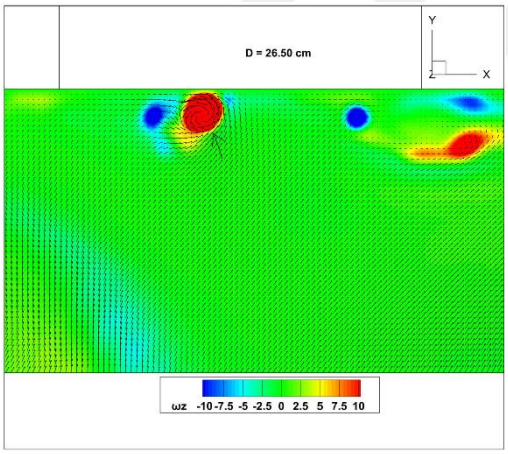

Figure A.12 Case-03 z-axis vorticity (ωz, 1/sec) slightly beneath the observable vortex core

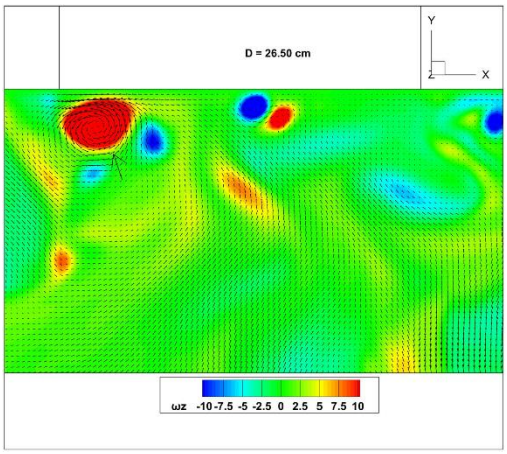

Figure A.13 Case-03 z-axis vorticity (ωz, 1/sec) at mid-S_c level (55.75 cm)

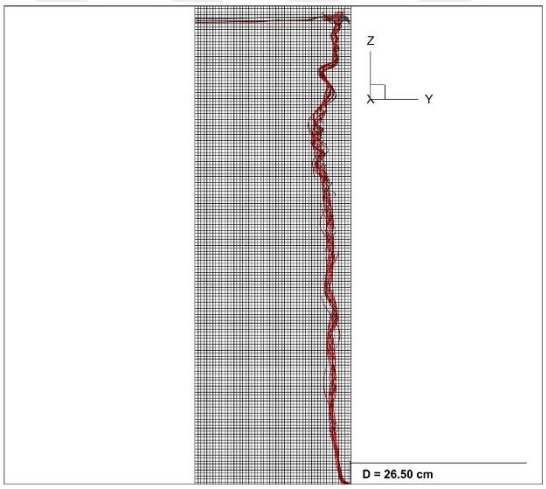

Figure A.14 Case-03 3D streamlines and isosurfaces of the air-water interface cross-section (longitudinal (y) direction)

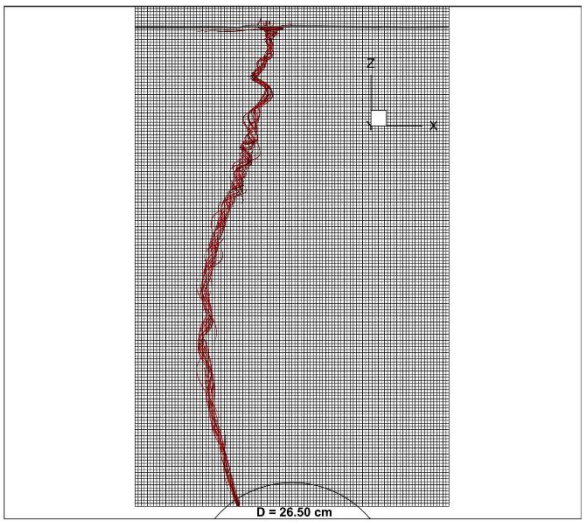

Figure A.15 Case-03 3D streamlines and isosurfaces of the air-water interface cross-section (transverse (x) direction)

Case-04: Single Intake with D = 26.50 cm, b = 120.00 cm, Q = 123.61 l/s, free water elevation = 67.50 cm

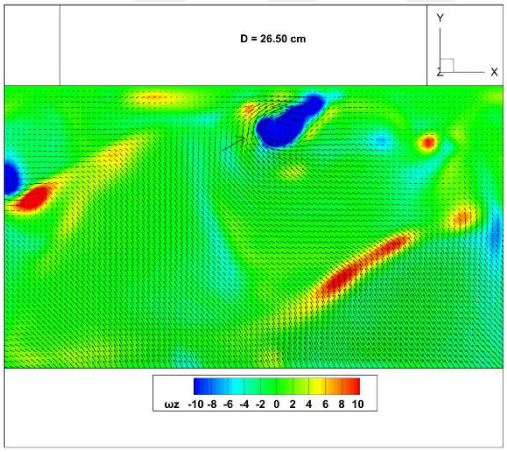

Figure A.16 Case-4 z-axis vorticity (ωz, 1/sec) at the free water surface

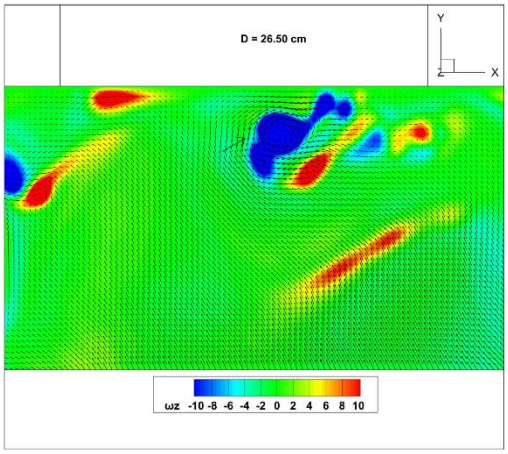

Figure A.17 Case-04 z-axis vorticity (ωz, 1/sec) slightly beneath the observable vortex core

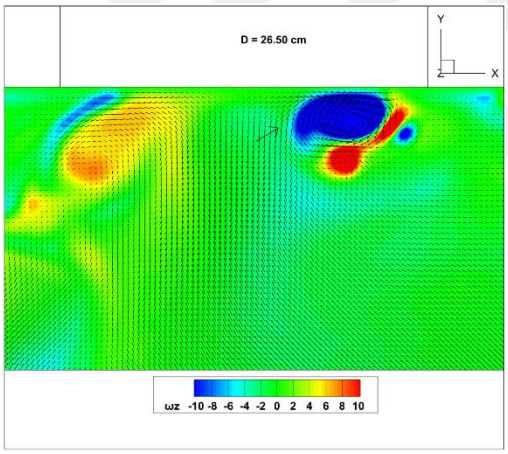

Figure A.18 Case-04 z-axis vorticity (ωz, 1/sec) at mid-S_c level (47.00 cm)

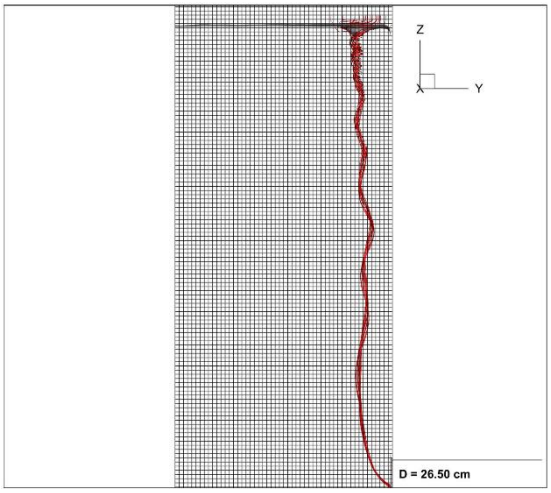

Figure A.19 Case-04 3D streamlines and isosurfaces of the air-water interface cross-section (longitudinal (y) direction)

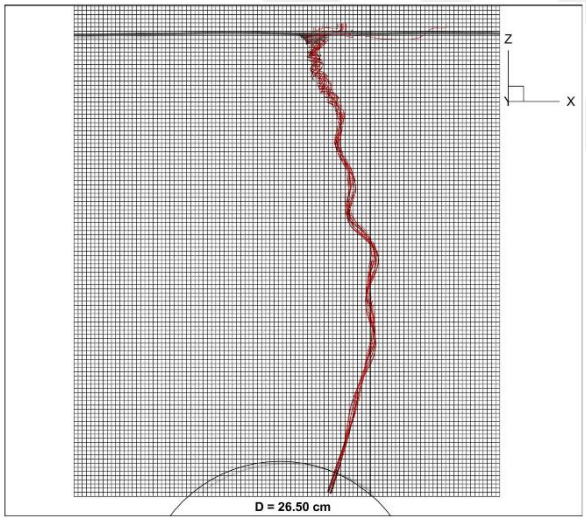

Figure A.20 Case-004 3D streamlines and isosurfaces of the air-water interface cross-section (transverse (x) direction)

Case-05: Single Intake with D = 26.50 cm, b = 120.00 cm,

Q = 110.14 l/s, free water elevation = 67.50 cm

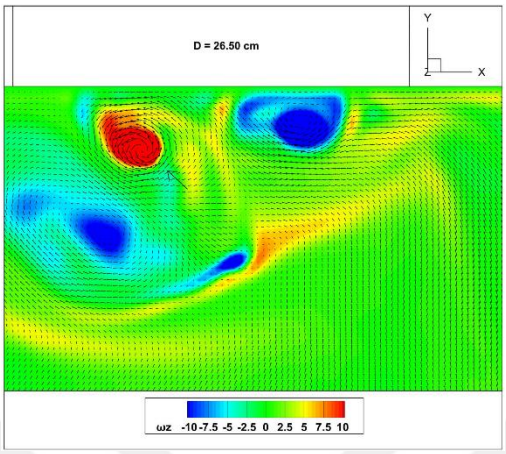

Figure A.21 Case-05 z-axis vorticity (ωz, 1/sec) at the free water surface

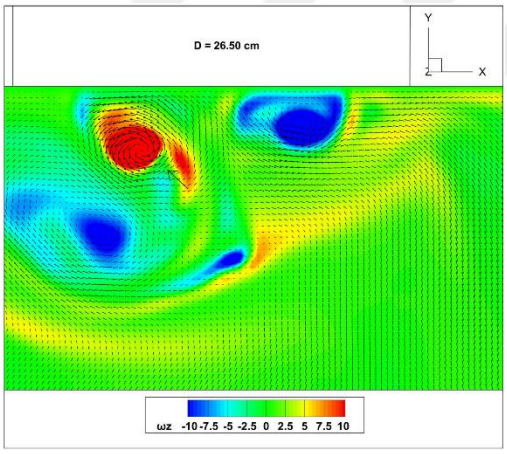

Figure A.22 Case-05 z-axis vorticity (ωz, 1/sec) slightly beneath the observable vortex core

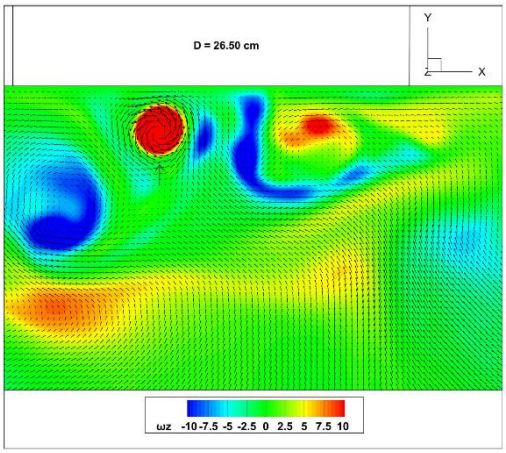

Figure A.23 Case-05 z-axis vorticity (ωz, 1/sec) at mid-S_c level (47.00 cm)

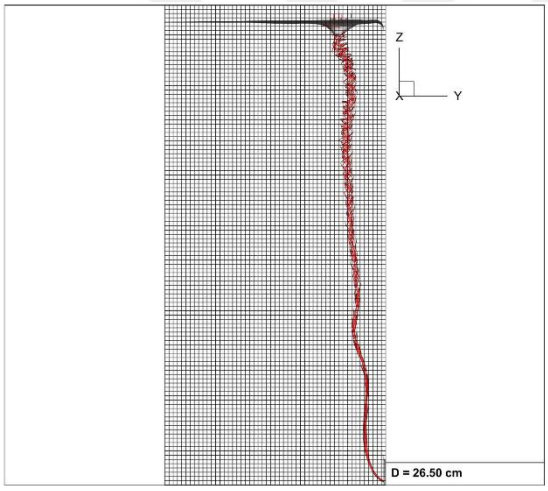

Figure A.24 Case-05 3D streamlines and isosurfaces of the air-water interface cross-section (longitudinal (y) direction)

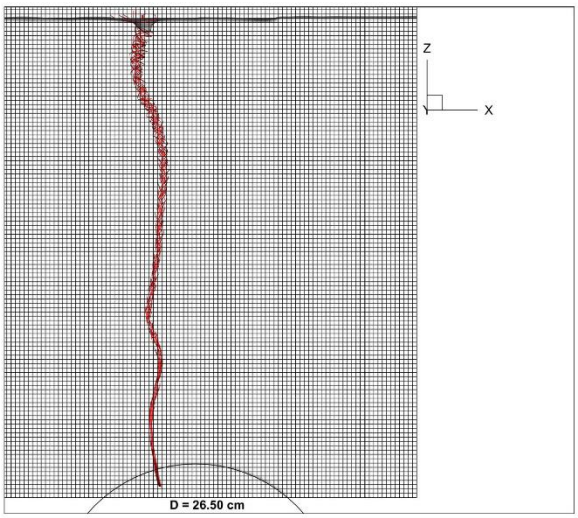

Figure A.25 Case-05 3D streamlines and isosurfaces of the air-water interface cross-section (transverse (x) direction)

Case-06: Double Intake with D = 26.50 cm, b = 120.00 cm, Q = 122.69 l/s, free water elevation = 60.00 cm

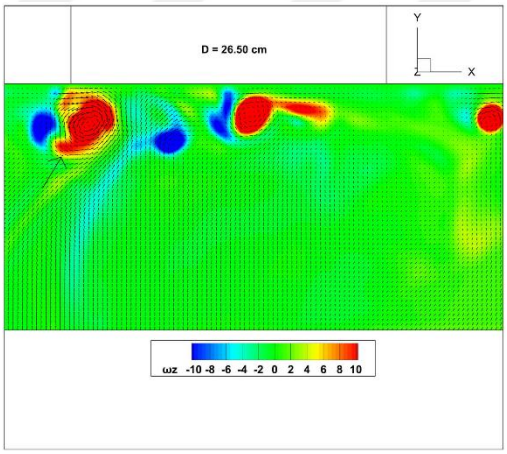

Figure A.26 Case-06 z-axis vorticity (ωz, 1/sec) at the free water surface

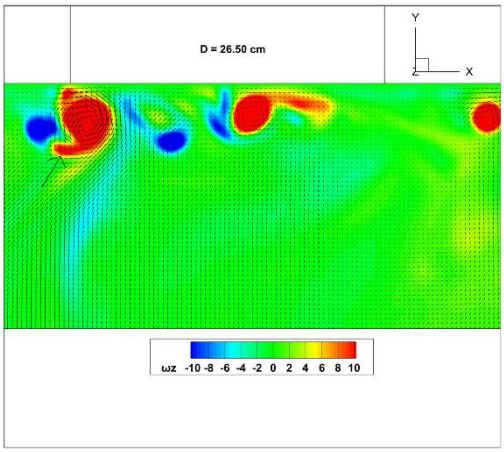

Figure A.27 Case-06 z-axis vorticity (ωz, 1/sec) slightly beneath the observable vortex core

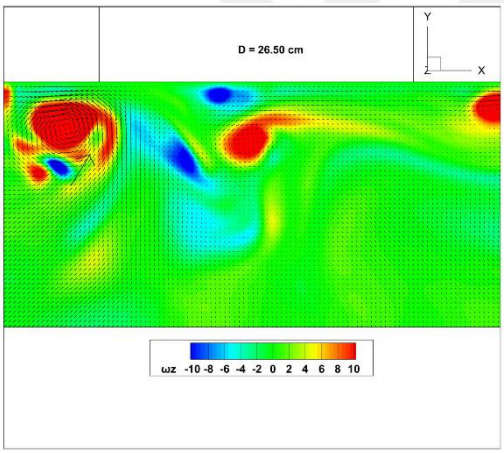

Figure A.28 Case-06 z-axis vorticity (ωz, 1/sec) at mid-S_c level (43.25 cm)

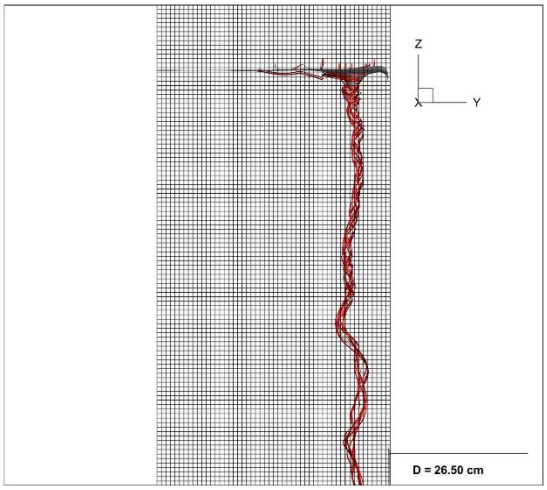

Figure A.29 Case-06 3D streamlines and isosurfaces of the air-water interface cross-section (longitudinal (y) direction)

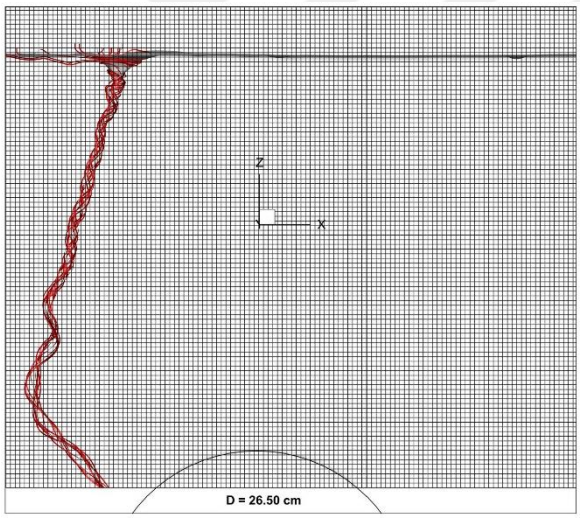

Figure A.30 Case-06 3D streamlines and isosurfaces of the air-water interface cross-section (transverse (x) direction)

Case-07: Double Intake with D = 26.50 cm, b = 120.00 cm,

Q = 110.04 l/s, free water elevation = 55.00 cm

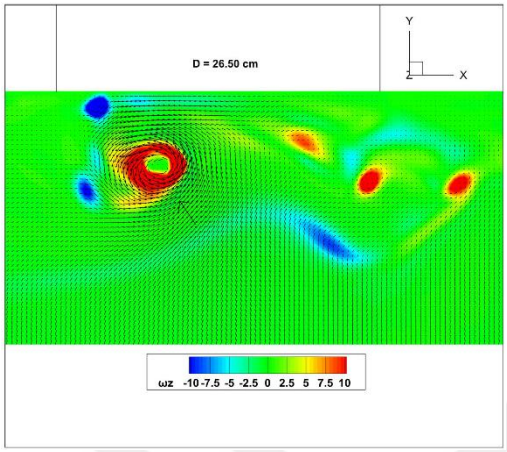

Figure A.31 Case-07 z-axis vorticity (ωz, 1/sec) at the free water surface

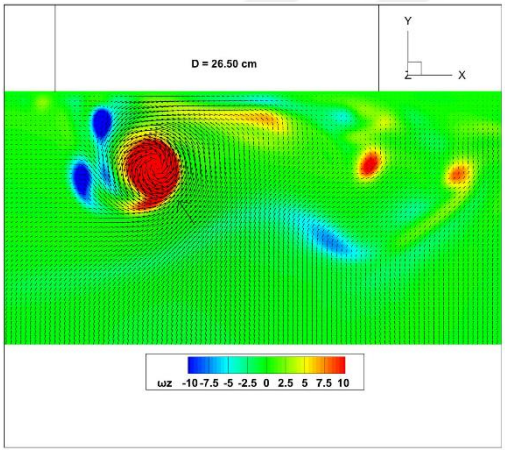

Figure A.32 Case-07 z-axis vorticity (ωz, 1/sec) slightly beneath the observable vortex core

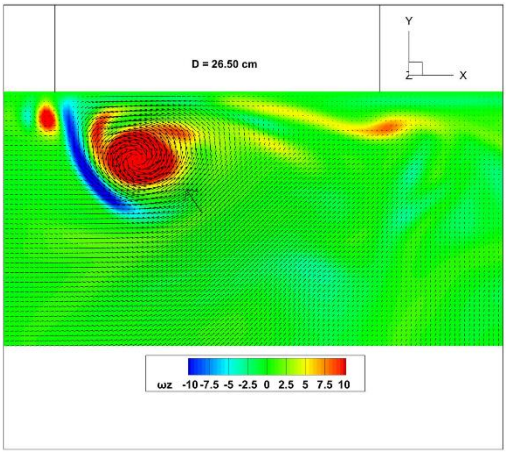

Figure A.33 Case-07 z-axis vorticity (ωz, 1/sec) at mid-S_c level (40.75 cm)

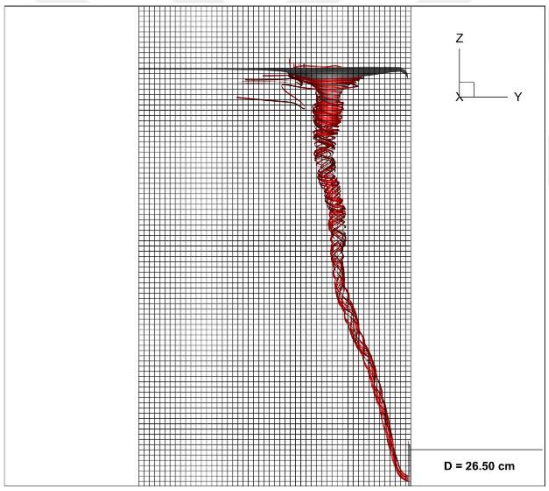

Figure A.34 Case-07 3D streamlines and isosurfaces of the air-water interface cross-section (longitudinal (y) direction)

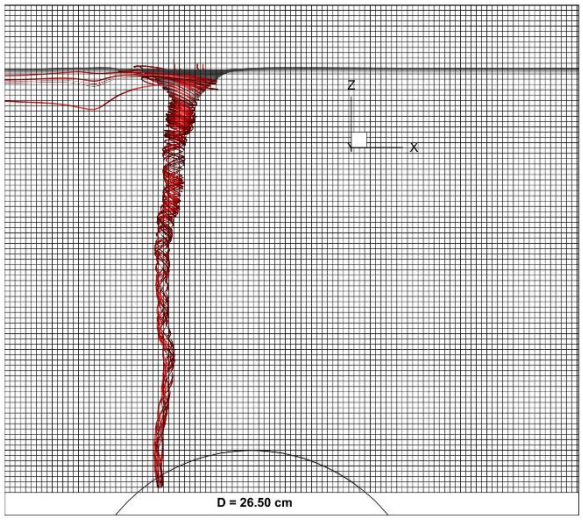

Figure A.35 Case-07 3D streamlines and isosurfaces of the air-water interface cross-section (transverse (x) direction)

Case-08: Double Intake with D = 26.50 cm, b = 120.00 cm, Q = 96.79 l/s, free water elevation = 50.00 cm

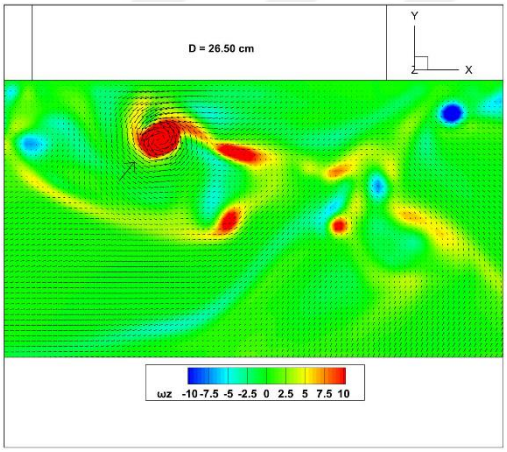

Figure A.36 Case-08 z-axis vorticity (ωz, 1/sec) at the free water surface

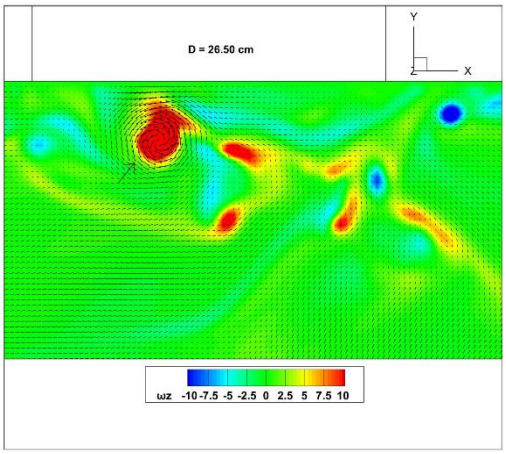

Figure A.37 Case-08 z-axis vorticity (ωz, 1/sec) slightly beneath the observable vortex core

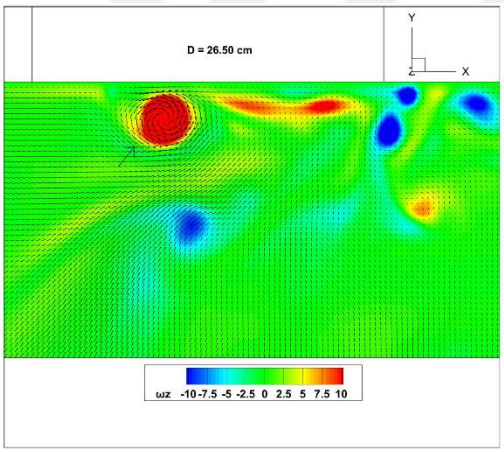

Figure A.38 Case-08 z-axis vorticity (ωz, 1/sec) at mid-S_c level (38.25 cm)

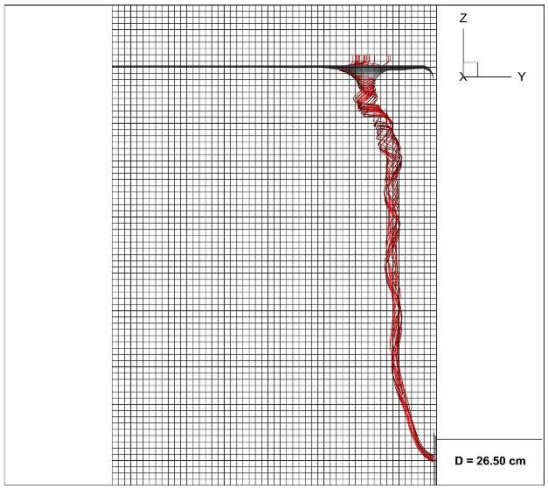

Figure A.39 Case-08 3D streamlines and isosurfaces of the air-water interface cross-section (longitudinal (y) direction)

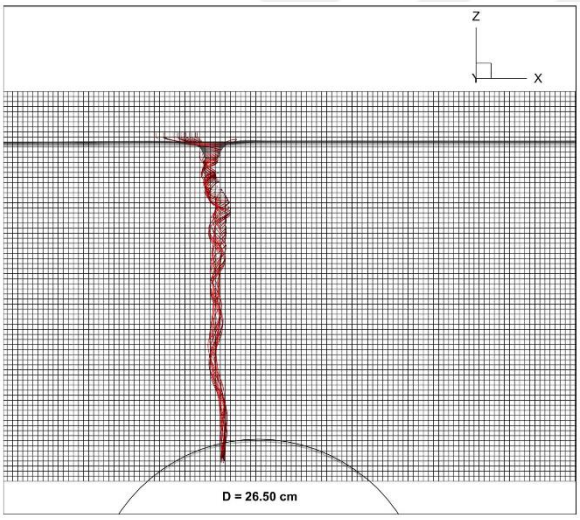

Figure A.40 Case-08 3D streamlines and isosurfaces of the air-water interface cross-section (transverse (x) direction)

Case-09: Double Intake with D = 26.50 cm, b = 120.00 cm,

Q = 88.21 l/s, free water elevation = 47.50 cm

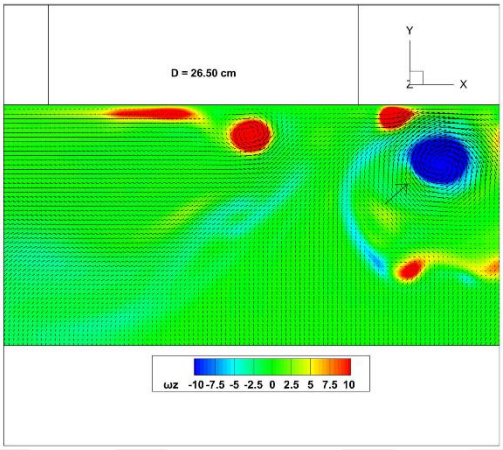

Figure A.41 Case-09 z-axis vorticity (ωz, 1/sec) at the free water surface

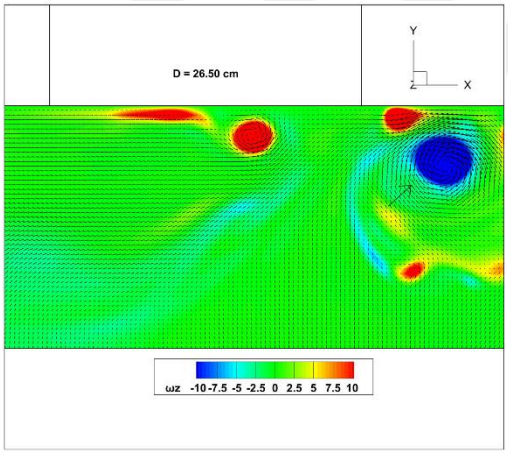

Figure A.42 Case-09 z-axis vorticity (ωz, 1/sec) slightly beneath the observable vortex core

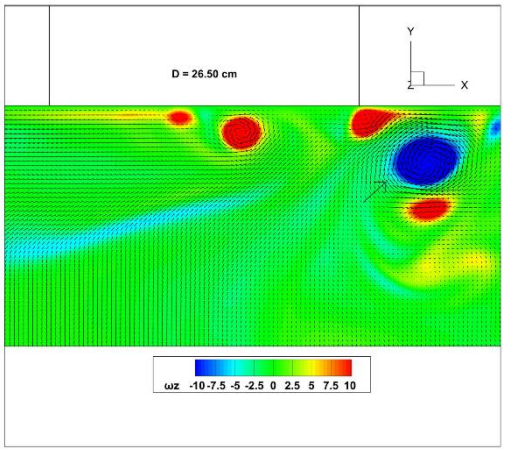

Figure A.43 Case-09 z-axis vorticity (ωz, 1/sec) at mid-S_c level (37.00 cm)

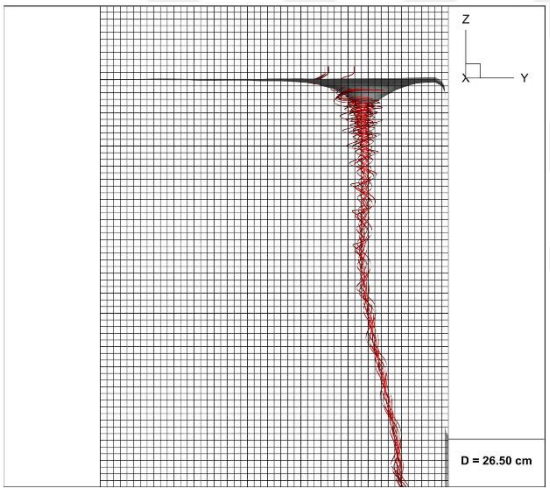

Figure A.44 Case-09 3D streamlines and isosurfaces of the air-water interface cross-section (longitudinal (y) direction)

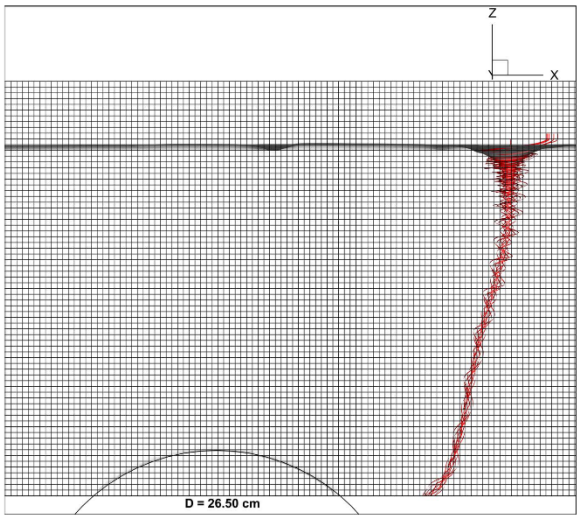

Figure A.45 Case-09 3D streamlines and isosurfaces of the air-water interface cross-section (transverse (x) direction)

Case-10: Double Intake with D = 26.50 cm, b = 120.00 cm, Q = 75.08 l/s, free water elevation = 42.50 cm

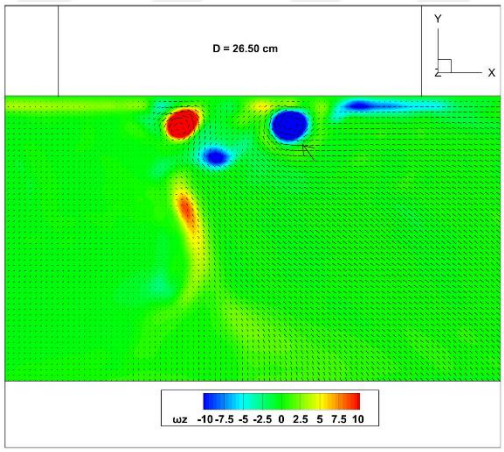

Figure A.46 Case-10 z-axis vorticity (ωz, 1/sec) at the free water surface

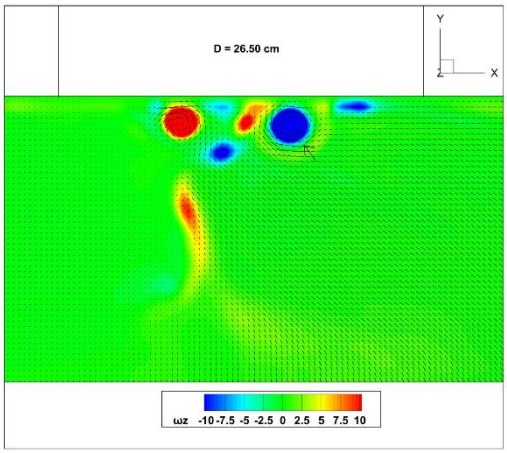

Figure A.47 Case-10 z-axis vorticity (ωz, 1/sec) slightly beneath the observable vortex core

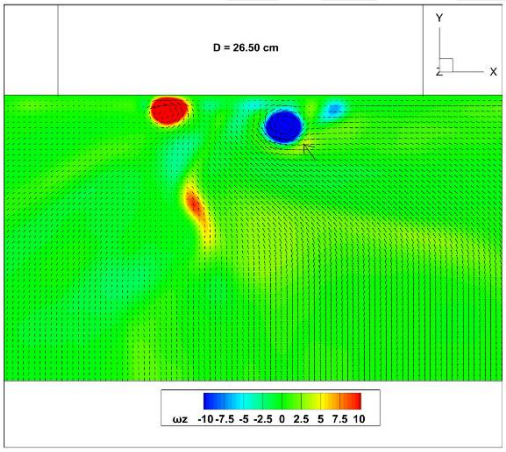

Figure A.48 Case-10 z-axis vorticity (ωz, 1/sec) at mid-S_c level (34.50 cm)

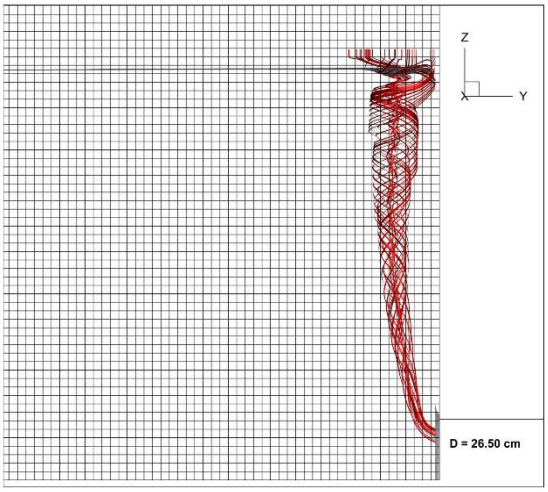

Figure A.49 Case-10 3D streamlines and isosurfaces of the air-water interface cross-section (longitudinal (y) direction)

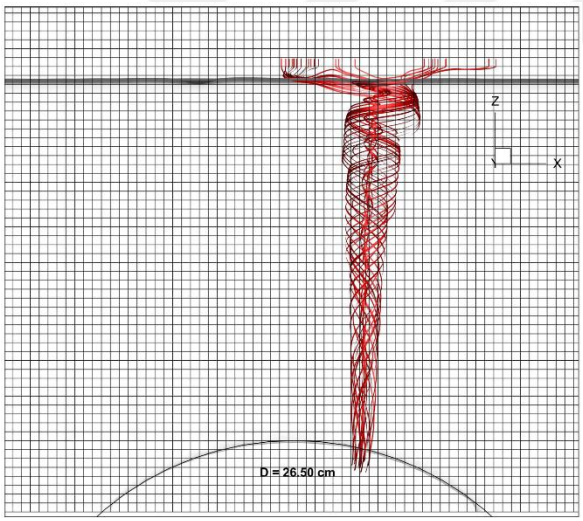

Figure A.50 Case-10 3D streamlines and isosurfaces of the air-water interface cross-section (transverse (x) direction)

Case-11: Triple Intake with D = 26.50 cm, b = 120.00 cm,

Q = 135.00 l/s, free water elevation = 65.00 cm

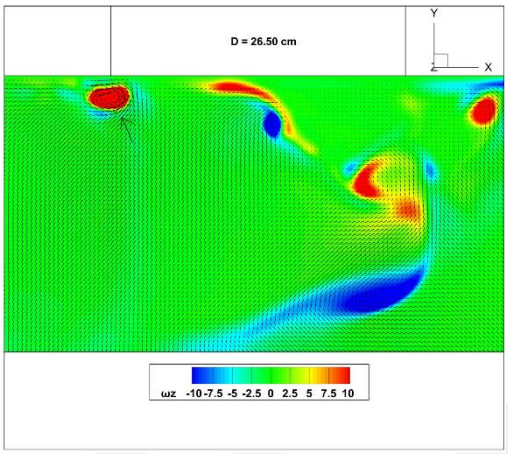

Figure A.51 Case-11 z-axis vorticity (ωz, 1/sec) at the free water surface

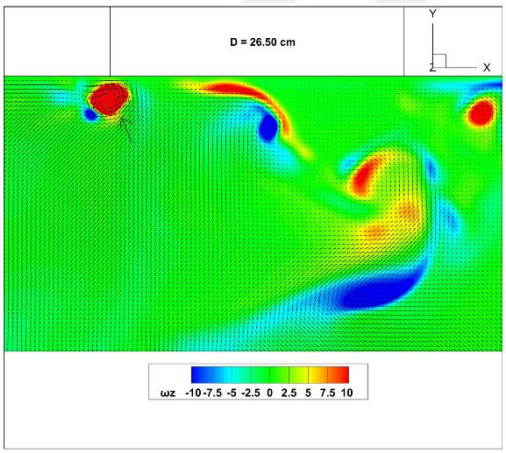

Figure A.52 Case-11 z-axis vorticity (ωz, 1/sec) slightly beneath the observable vortex core

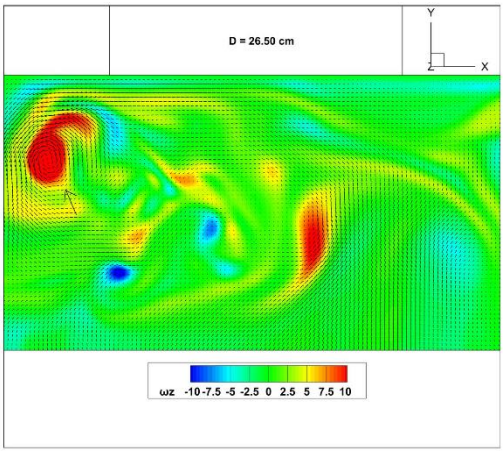

Figure A.53 Case-11 z-axis vorticity (ωz, 1/sec) at mid-S_c level (45.75 cm)

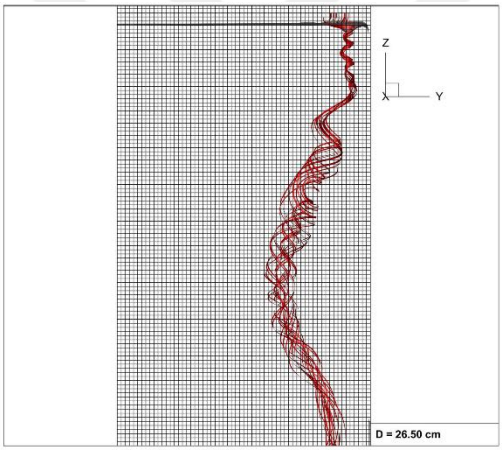

Figure A.54 Case-11 3D streamlines and isosurfaces of the air-water interface cross-section (longitudinal (y) direction)

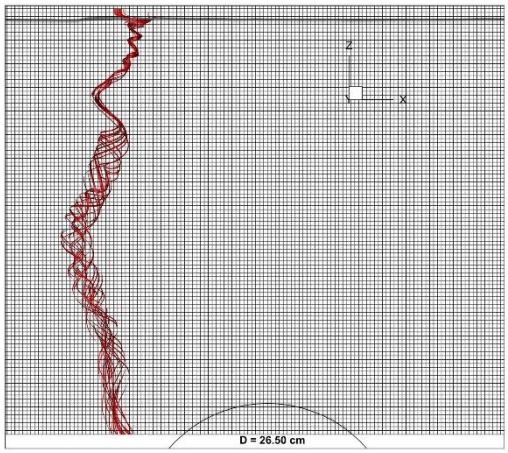

Figure A.55 Case-11 3D streamlines and isosurfaces of the air-water interface cross-section (transverse (x) direction)

Case-12: Triple Intake with D = 26.50 cm, b = 120.00 cm, Q = 122.69 l/s, free water elevation = 62.50 cm

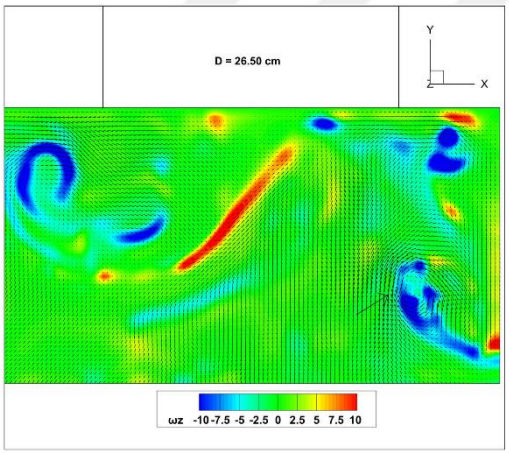

Figure A.56 Case-12 z-axis vorticity (ωz, 1/sec) at the free water surface

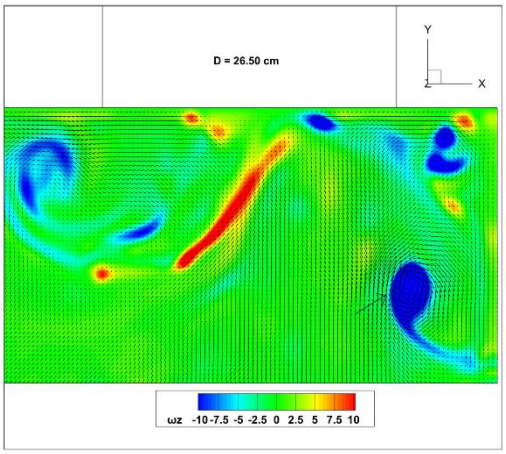

Figure A.57 Case-12 z-axis vorticity (ωz, 1/sec) slightly beneath the observable vortex core

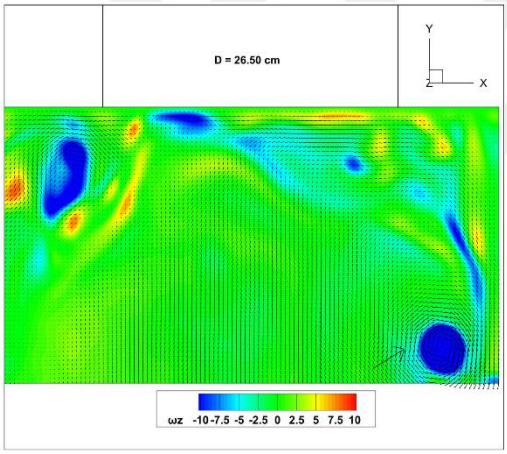

Figure A.58 Case-12 z-axis vorticity (ωz, 1/sec) at mid-S_c level (44.50 cm)

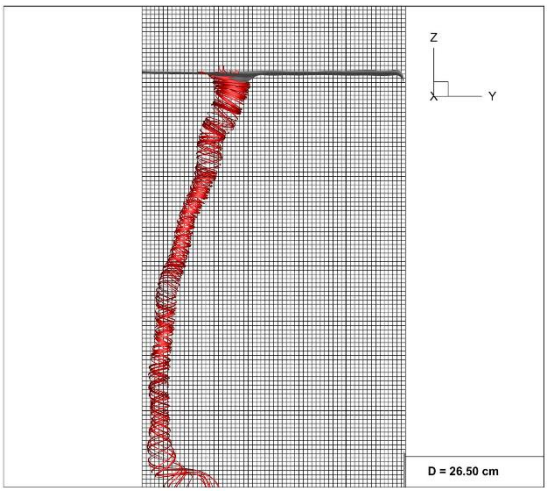

Figure A.59 Case-12 3D streamlines and isosurfaces of the air-water interface cross-section (longitudinal (y) direction)

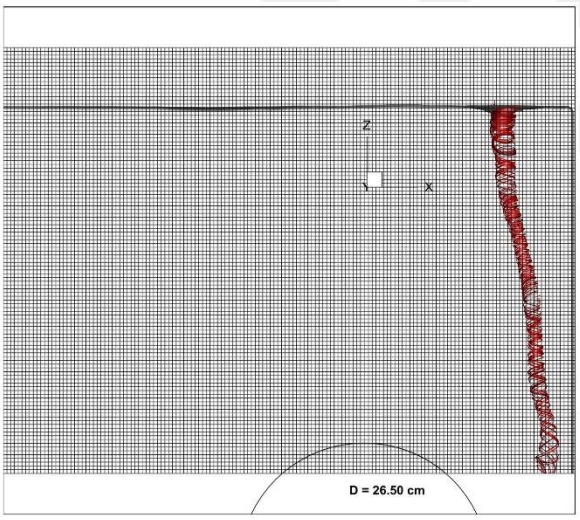

Figure A.60 Case-12 3D streamlines and isosurfaces of the air-water interface cross-section (transverse (x) direction)

Case-13: Triple Intake with D = 26.50 cm, b = 120.00 cm,

Q = 110.04 l/s, free water elevation = 57.50 cm

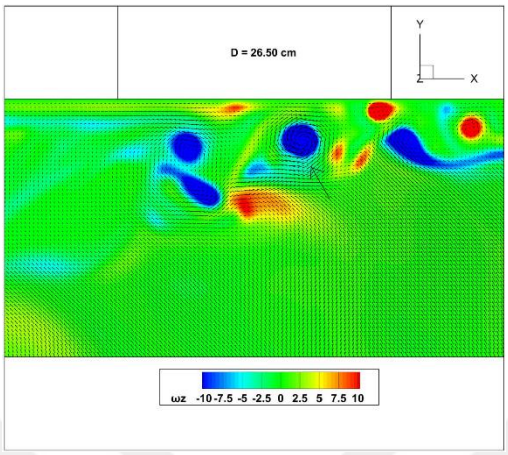

Figure A.61 Case-13 z-axis vorticity (ωz, 1/sec) at the free water surface

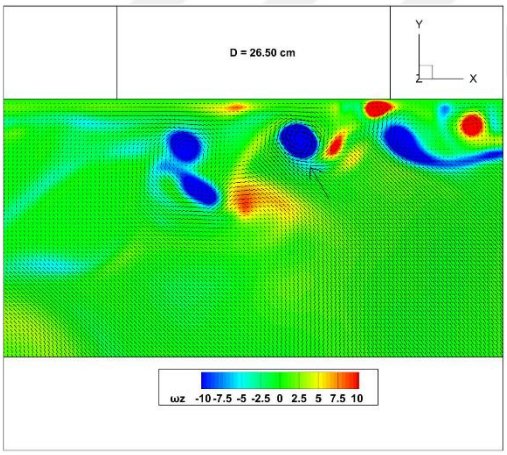

Figure A.62 Case-13 z-axis vorticity (ωz, 1/sec) slightly beneath the observable vortex core

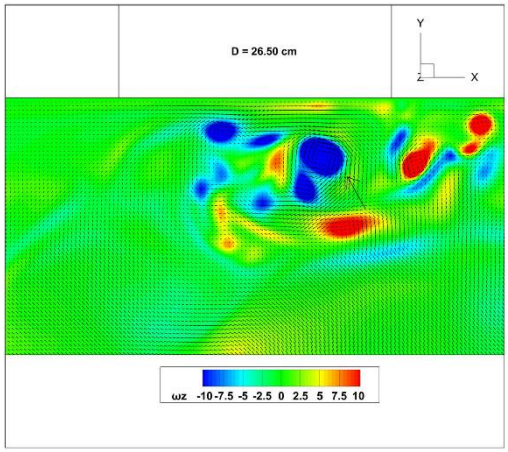

Figure A.63 Case-13 z-axis vorticity (ωz, 1/sec) at mid-S_c level (42.00 cm)

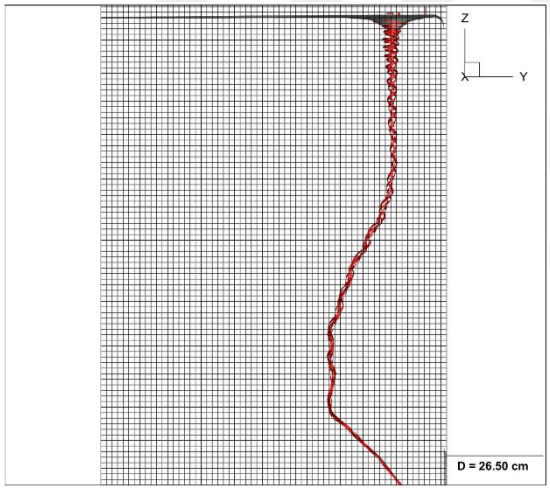

Figure A.64 Case-13 3D streamlines and isosurfaces of the air-water interface cross-section (longitudinal (y) direction)

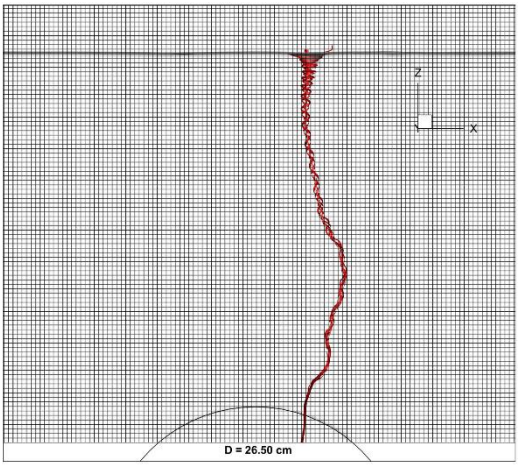

Figure A.65 Case-13 3D streamlines and isosurfaces of the air-water interface cross-section (transverse (x) direction)

Case-14: Triple Intake with D = 26.50 cm, b = 120.00 cm, Q = 96.79 l/s, free water elevation = 50.00 cm

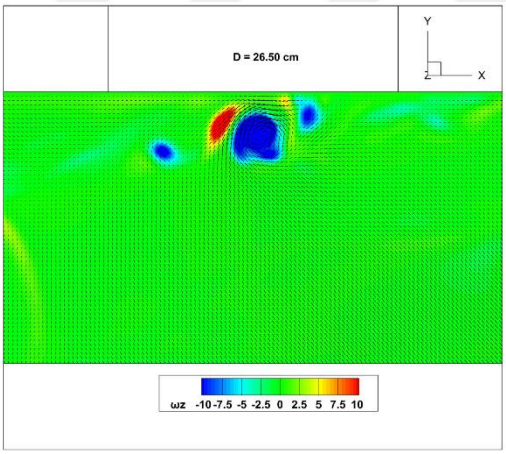

Figure A.66 Case-14 z-axis vorticity (ωz, 1/sec) at the free water surface

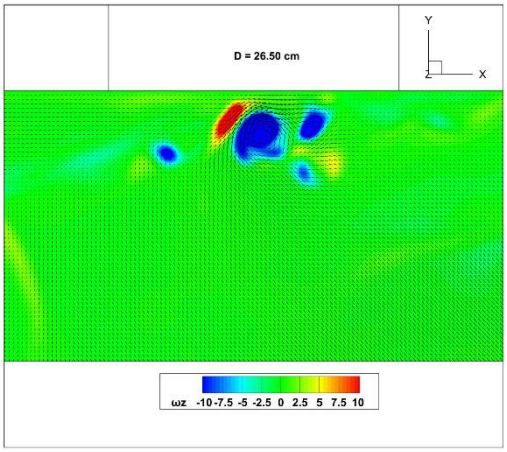

Figure A.67 Case-14 z-axis vorticity (ωz, 1/sec) slightly beneath the observable vortex core

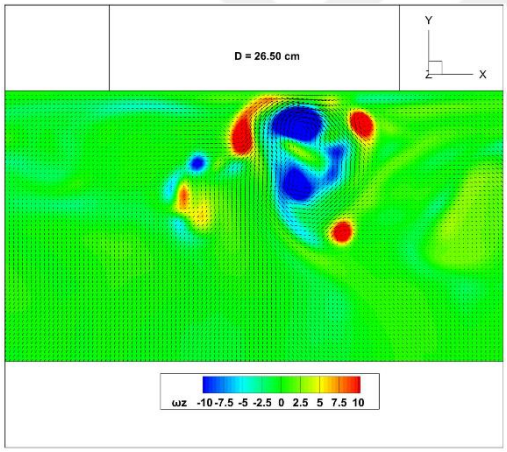

Figure A.68 Case-14 z-axis vorticity (ωz, 1/sec) at mid-S_c level (38.25 cm)

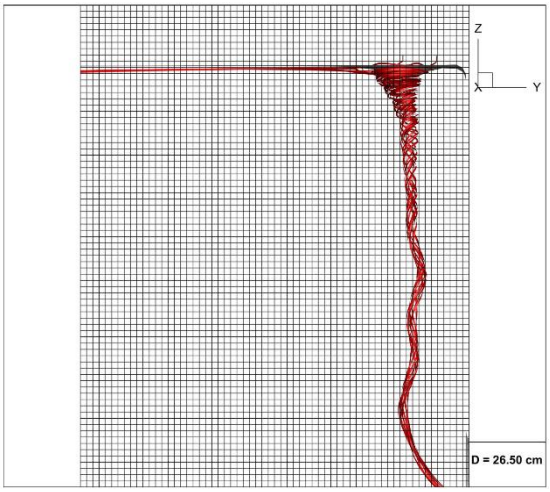

Figure A.69 Case-14 3D streamlines and isosurfaces of the air-water interface cross-section (longitudinal (y) direction)

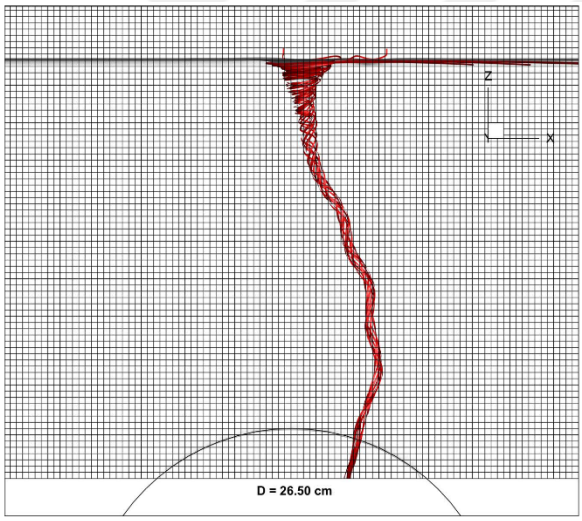

Figure A.70 Case-14 3D streamlines and isosurfaces of the air-water interface cross-section (transverse (x) direction)

Case-15: Triple Intake with D = 26.50 cm, b = 120.00 cm,

Q = 87.96 l/s, free water elevation = 50.00 cm

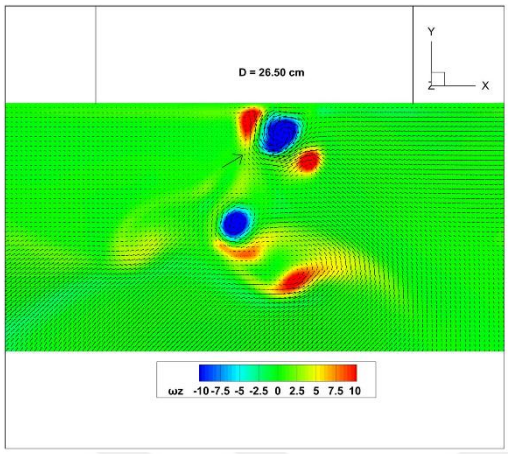

Figure A.71 Case-15 z-axis vorticity (ωz, 1/sec) at the free water surface

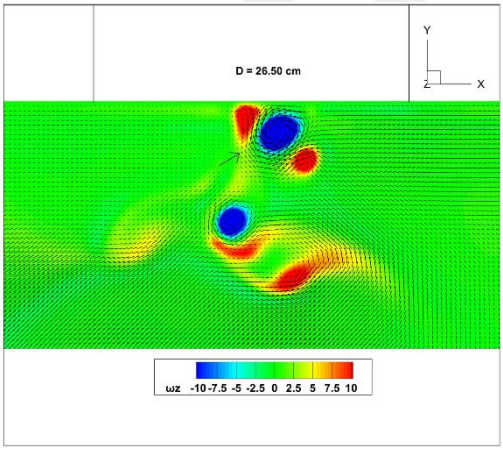

Figure A.72 Case-15 z-axis vorticity (ωz, 1/sec) slightly beneath the observable vortex core

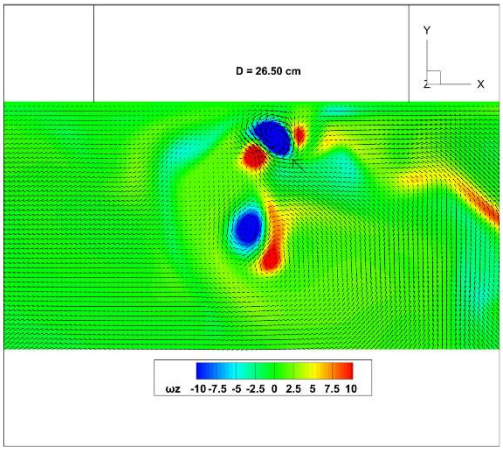

Figure A.73 Case-15 z-axis vorticity (ωz, 1/sec) at mid-S_c level (38.25 cm)

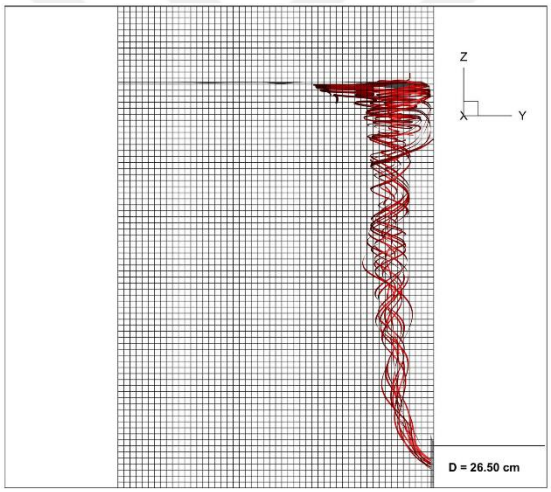

Figure A.74 Case-15 3D streamlines and isosurfaces of the air-water interface cross-section (longitudinal (y) direction)

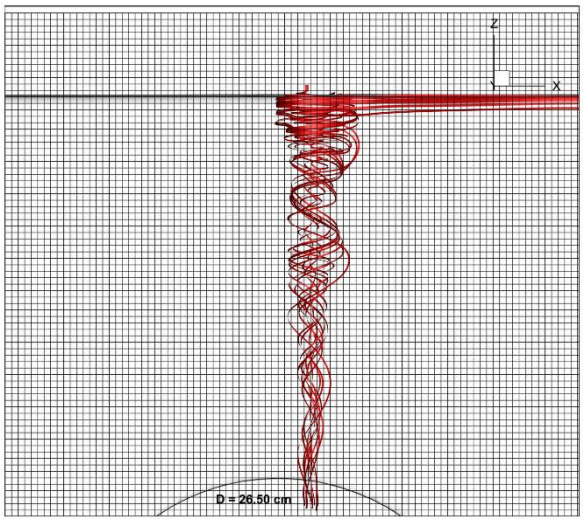

Figure A.75 Case-15 3D streamlines and isosurfaces of the air-water interface cross-section (transverse (x) direction)